Journal of
Materials Chemistry B

ROYAL SOCIETY
OF CHEMISTRY

COMMUNICATION

View Article Online
View Journal

Cite this: DOI: 10.1039/d5tb02866c

Received 20th December 2025,
Accepted 21st April 2026

DOI: 10.1039/d5tb02866c

rsc.li/materials-b

Innovative design of fluorescent PLGA–1,8-naphthalimide nanoparticles as multifunctional materials for next-generation nanotechnology and biomedicine

Yuriev Danil,[a] Tkachenko Sergey,[a] Ermolin Danila,[b] Ivanov Ilya,[bk] Melnikov Pavel,[c] Malinovskaya Julia,[a] Ryabova Anastasia,[def] Mishin Alexander,[g] Perfilov Maxim,[g] Ramil Khasbiullin,[h] Medvedev Michael,[bk] Skorb Ekaterina,[b] Oshchepkov Maxim,[a] Gelperina Svetlana[a] and Oshchepkov Alexander *[ij]

Poly(lactic-*co*-glycolic acid) (PLGA)-based nanoparticles featuring covalently incorporated 1,8-naphthalimide fluorophores were developed through DFT/TD-DFT-guided molecular engineering. Systematic variation of 4-position substituents and carbon spacer lengths established clear structure–property relationships governing spectral–luminescent characteristics and conjugate stability. Computational modeling accurately predicted experimental absorption/emission features. The optimized PLGA-fluorophore conjugates yielded nanoparticles with high aqueous fluorescence, excellent colloidal stability, and approximately two-fold higher photostability than PLGA–Cy5 under the tested imaging conditions. Live-cell confocal microscopy (405 nm excitation) demonstrated strong emission and homogeneous distribution in 4T1/HeLa cells, confirming suitability for *in vitro* cellular imaging with high cell viability. This covalent PLGA labeling platform establishes a quantifiable foundation for advanced fluorescent nanomaterials in cellular imaging applications. While these results establish a robust platform for cellular imaging applications, extended *in vivo* validation remains a goal for future work.

Introduction

The rational design of polymer-based drug delivery systems (DDS) has entered a transformative stage powered by computational chemistry, where predictive modeling tools enable precise control over polymer architecture, interfacial dynamics, and multiscale interactions.[1,2] Among these methods, density functional theory (DFT) has become an indispensable component of materials discovery, allowing quantitative insight into electronic structure, intermolecular interactions, and dynamic behaviors in multi-component polymer systems.[3] The integration of DFT-driven design with synthetic polymer chemistry is redefining how biodegradable materials are conceptualized for drug delivery and nanomedicine.

Among biodegradable polymers, poly(lactic-*co*-glycolic acid) (PLGA) stands as a cornerstone of clinical translation and regulatory success, underpinning more than 25 FDA- and EMA-approved therapeutics, including long-acting injectables and implantable delivery systems.[4–6] PLGA's hydrolytic degradability, tunable composition, and terminal carboxyl/hydroxyl groups enable covalent functionalization with ligands, chelators, or fluorescent reporters - essential for controlled release, targeting, and visualization.[7–13]

However, predicting functionalization effects on polymer properties remains challenging. Experimental screening alone cannot map complex parameter spaces; DFT thus emerges as a predictive strategy for conjugation sites and substituents that preserve stability and function.

---

[a] *Mendeleev University of Chemical Technology of Russia, Miusskaya pl., 9, Moscow, 125047, Russian Federation*
[b] *Infochemistry Scientific Center, ITMO University, 9 Lomonosova Str., St. Petersburg, 191002, Russian Federation*
[c] *Rudolf Virchow Center, Center for Integrative and Translational Bioimaging, University of Wuerzburg, Josef-Schneider-Str. 2, Würzburg, 97080, Germany*
[d] *Prokhorov General Physics Institute of the Russian Academy of Sciences, Vavilov Str. 38, Moscow, 119991, Russian Federation*
[e] *National Research Nuclear University MEPHI, Kashirskoye Highway 31, Moscow, 115409, Russian Federation*
[f] *RUDN University, Miklukho-Maklaya str. 6, Moscow, 117198, Russian Federation*
[g] *Shemyakin-Ovchinnikov Institute of Bioorganic Chemistry, RAS (IBCh RAS), Miklukho-Maklaya 16/10, Moscow, 117997, Russian Federation*
[h] *Frumkin Institute of Physical Chemistry and Electrochemistry Russian Academy of Sciences (IPCE RAS), 31-4, Leninsky prospect, Moscow, 119071, Russian Federation*
[i] *Martin Luther University Halle-Wittenberg, Kurt-Mothes-Straße 2, D-06120 Halle, Germany. E-mail: alexander.oshchepkov@chemie.uni-halle.de*
[j] *Max Planck Institute for the Science of Light, Department of Physics, D-91058 Erlangen, Germany*
[k] *N.D. Zelinsky Institute of Organic Chemistry of Russian Academy of Sciences, 119991 Moscow, Russian Federation*

Fluorescent labelling is critical for nanocarrier visualization,[14,15] yet physical dye entrapment causes leaching, photobleaching, and signal variability.[16,17] Covalent conjugation mitigates these but risks polymer disruption.[18] Few fluorophores combine strong aqueous emission with stability against quenchers (*e.g.*, Fe^{3+}, Zn^{2+}, Cu^{2+}, pH shifts).

1,8-Naphthalimide derivatives excel here, offering high quantum yields ($\Phi > 0.8$), photostability, and tunable emission across the visible spectrum.[19–22] Their chemical rigidity and small steric footprint minimize disruption of PLGA crystallinity and degradation kinetics, preserving the balance between optical function and polymer matrix integrity.[23] DFT simulations further confirm that covalent modification of PLGA with 1,8-naphthalimides does not induce significant electronic perturbations within the dye's aromatic core or the polymer backbone orbitals, indicating that the intrinsic photophysical properties of the fluorophore remain largely conserved in the conjugate.[24–27]

Building on these insights, the present study establishes a DFT-guided design strategy for developing fluorescent PLGA–1,8-naphthalimide conjugates with controlled structural and optical characteristics. Two series of amino-functionalized 1,8-naphthalimide derivatives – differing in substituents at the 4-position of the aromatic ring and spacer length – were synthesized and covalently coupled to PLGA, yielding monodisperse nanoparticles (NPs) *via* controlled nanoprecipitation.[28,29] Spectroscopic analysis demonstrated that the conjugation preserved the spectral–luminescent properties of the free dyes, with absorption maxima in the 350–450 nm range and quantum yields exceeding 0.75, validated by DFT predictions. The resulting nanoparticles exhibited excellent colloidal stability, pronounced fluorescence intensity, and consistent emission across biological conditions, enabling precise tracking within both murine 4T1 and transfected HeLa cell lines.

Due to their photostability and emission consistency, these 1,8-naphthalimide-based PLGA conjugates hold strong potential for targeted drug delivery, diagnostic imaging, and super-resolution microscopy.[30–32] This integration of DFT-driven modeling, molecular synthesis, and nanotechnological engineering provides a predictive framework for structure–property relationships and a foundation for optically traceable polymeric nanocarriers, bridging polymer chemistry, photophysics, and biomedical imaging toward multifunctional theranostic systems.

Results and discussion

New 1,8-naphthalimide derivatives as markers for fluorescent delivery systems

Recent advances in dye chemistry have intensified research into 1,8-naphthalimide derivatives, which combine structural simplicity with highly advantageous photophysical characteristics.[33–35] These compounds exhibit strong spectral luminescence, excellent photostability, low cytotoxicity, and tunable emission profiles extending from blue to red regions of the visible spectrum, depending on the electronic nature of the substituents attached to the naphthalimide core.[36] Their relatively simple molecular architecture, devoid of heavy multi-electron atoms, also makes them particularly suitable for accurate theoretical modeling. This enables correlation between molecular structure and optical properties using density functional theory (DFT), facilitating the rational design of fluorophores with predictable emission behavior.

Reported 1,8-naphthalimide derivatives generally emit in the blue (450–500 nm) and green (500–570 nm) spectral regions. Importantly, these wavelengths fall within the optical window that is ideal for *in vitro* and *in vivo* visualization, where signal clarity and low background interference are critical. By operating within these regions, naphthalimide-based fluorophores can complement or even surpass traditional dyes, many of which emit at longer wavelengths and often face issues with stability and spectral overlap under biological conditions.

Building on this foundation, our research group previously developed two structurally related series of 1,8-naphthalimide derivatives optimized for fluorescent polymer conjugation.[37] The first series incorporated morpholine substituents at the 4-position of the aromatic nucleus (compounds **1–4**), producing dyes with emission maxima in the green spectral region. The second series introduced ethoxyethyl substituents at the same position (compounds **5–8**), resulting in blue-emitting analogues (Scheme 1). Within each series, the molecular design was further diversified by varying the length of the alkyl spacer linking the naphthalimide fluorophore to the terminal amino group. This amino functionality serves as a reactive site for covalent coupling to PLGA and other polymeric backbones, anchoring the dye in a defined orientation and enhancing fluorescence consistency in complex environments.

In the present study, these two derivative series are comprehensively examined to elucidate how the carbon spacer length influences the photophysical response and structural integration of the fluorophores into polymer matrices. This systematic approach not only provides a means to fine-tune the optical output but also reveals how subtle molecular modifications govern the balance between emission efficiency and chemical compatibility with biodegradable carriers. Ultimately, identifying the most spectrally stable and photochemically resistant naphthalimide derivatives paves the way for their deployment as reliable fluorescent markers in medical diagnostics, bioimaging, and polymer-based nanocarrier development.

Covalent modification of PLGA with fluorophores 1–8

Fluorophores can be introduced into PLGA-based polymer nanoparticles through two principal strategies: non-covalent encapsulation of hydrophobic dyes and covalent chemical modification of the polymer backbone. The non-covalent approach is widely used because of its procedural simplicity, compatibility with a broad range of dyes, and its ability to achieve high loading efficiencies within nanoparticles.[10,38] However, its practical utility in bioimaging and biodistribution studies is often limited by inadequate dye retention, dye diffusion into the surrounding medium, and unpredictable photobleaching under

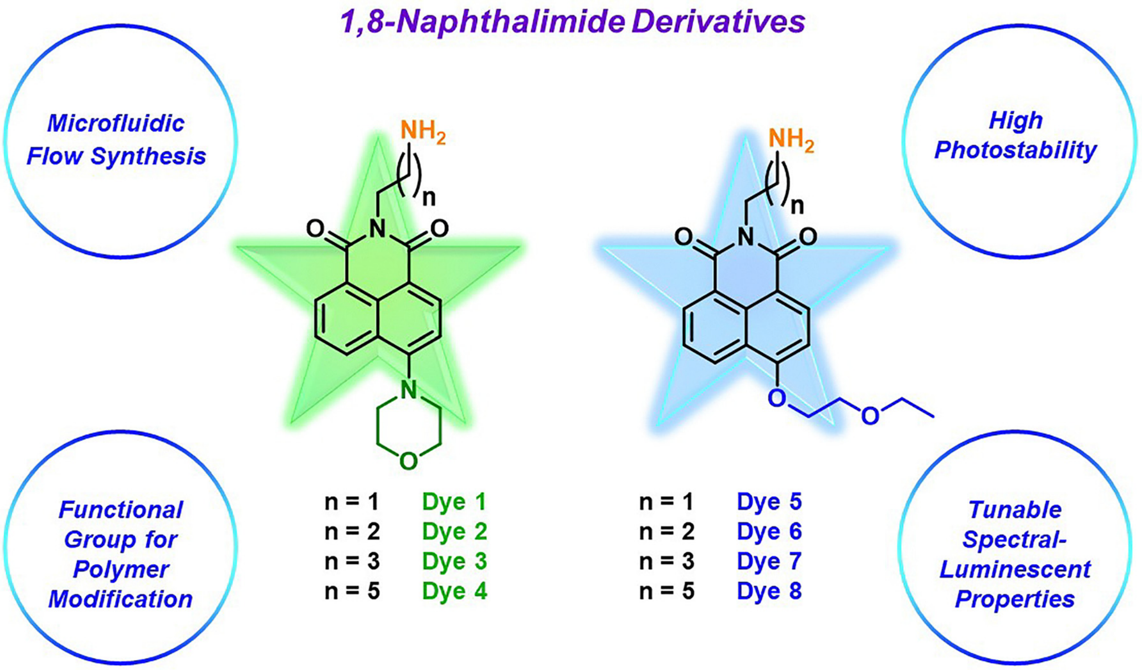

Scheme 1 Chemical structures of 1,8-naphthalimide derivatives 1–8 used in the study.

physiological conditions. These effects collectively impair fluorescence signal stability and make quantitative tracking of fluorescent nanocarriers unreliable in complex biological environments.

In contrast, covalent bonding of a fluorophore to the polymer chain provides a robust solution, significantly enhancing structural integrity, chemical stability, and signal reproducibility during imaging.[39] By anchoring the fluorescent moiety directly to the polymer backbone, the system effectively eliminates dye leaching while ensuring consistent optical output over extended observation periods. To exploit these advantages, we designed and synthesized a series of covalently modified PLGA polymers incorporating eight distinct 1,8-naphthalimide derivatives (compounds **1–8**), combining synthetic experimentation with density functional theory (DFT) modeling to elucidate how fluorophore structure affects conjugation efficiency and optical response.

The incorporation of 1,8-naphthalimide derivatives into the PLGA backbone confers several potential advantages over conventional fluorophores for covalent polymeric labeling. These include low steric hindrance facilitating efficient amide coupling (compared to bulky rhodamines), inherent hydrolytic stability that preserves fluorescence during PLGA degradation (unlike labile sulfonyl chloride dyes), enhanced photostability under prolonged illumination relative to FITC under the same imaging conditions, and tunable intramolecular charge transfer (ICT) without heavy-atom quenching effects. Table S1 (SI) provide comprehensive comparisons with established PLGA-fluorophore systems (fluorescein, Cy5, quantum dots). It should be noted that these comparisons are based on literature data and our own measurements under specific experimental conditions; systematic side-by-side benchmarking under identical settings would be required to establish general superiority.

Poly(lactic-*co*-glycolic acid) Resomer 502H was selected as the primary polymer matrix for this work due to its well-balanced lactide : glycolide ratio of 50 : 50 and the presence of free terminal carboxyl groups available for functionalization. The generic reaction scheme for covalent conjugation between PLGA and the aminated 1,8-naphthalimides is illustrated in Fig. 1. The derivatization proceeded *via* an amidation pathway between the polymer's terminal carboxyl group and the dye's amino group, employing the carbodiimide coupling strategy. All reactions were carried out under mild conditions, activating the polymer with *N*′-(3-dimethylaminopropyl)-*N*-ethylcarbodiimide (EDC) and *N*-hydroxysuccinimide (NHS), with catalytic diisopropylethylamine (DIPEA) serving as a base to facilitate ester activation.

Both dichloromethane and dimethylformamide proved suitable solvents for the amidation, providing solubility for all eight naphthalimide derivatives and ensuring homogeneous reaction conditions. The coupling reactions were conducted for 48 hours at ambient temperature, conditions chosen to minimize potential polymer degradation and preserve molecular weight. After completion, the modified polymers were purified by extraction, followed by precipitation in hexane through gradual addition of the polymer solution dissolved in minimal ethyl acetate. The resulting solids were collected by filtration and dried in air. Across all conjugates, the isolated yields ranged from 60 to 80%, demonstrating consistent reactivity of the PLGA matrix toward the different fluorophore derivatives.

Physicochemical characterization of PLGA–naphthalimide conjugates

To confirm the structure of the resulting conjugates, studies were conducted using a combination of physicochemical

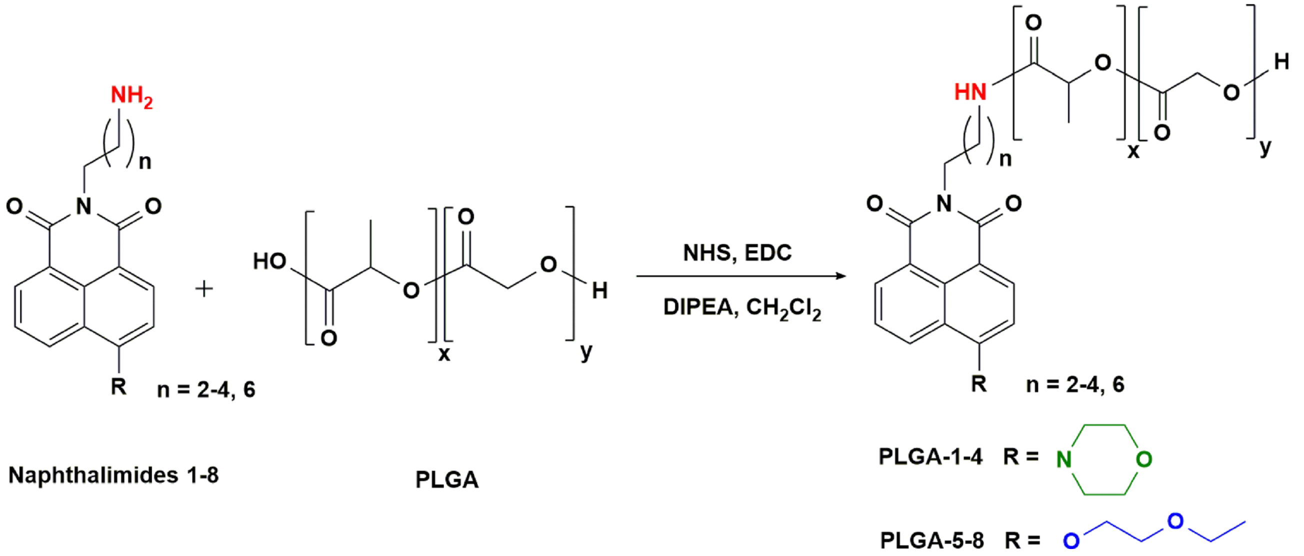

Fig. 1 Reaction of covalent modification of PLGA with 1,8-naphthalimide derivatives 1–8.

analysis methods. For example, when comparing the ^{1}H NMR spectra of unmodified PLGA and the PLGA-5 conjugate (Fig. S1–S4, SI), peaks corresponding to the aromatic ring of 1,8-naphthalimide are present in the downfield region at 7.7–8.7 ppm. Fig. S5 (SI) shows the IR spectra of unmodified PLGA and the PLGA-5 conjugate. The spectra exhibit typical bands at 1087 cm^{-1}, 1167 cm^{-1}, and 1748 cm^{-1}, attributed to C═O stretching vibrations and asymmetric and symmetric C–O stretching vibrations of the PLGA ester chain, as well as bands due to C–H stretching vibrations of methylene units at approximately 2951 cm^{-1}. The bands and similarities between the two spectra demonstrate that the PLGA backbone remains unchanged and unmodified. New peaks appeared in the spectrum of the PLGA-**5** conjugate, namely a band at 1543 cm^{-1}, corresponding to the NH vibrations of the amide group, and a band at 1682 cm^{-1}, associated with the C═O stretching vibrations of the amide group. Thus, the IR spectroscopy data confirm the conjugation of the naphthalimide dye with the formation of an amide bond between the carboxyl group of the polymer and the primary amino group of 1,8-naphthalimide.

Also, using gel permeation chromatography, analysis of PLGA and PLGA-**5** samples was performed using a UV detector (Fig. S6, SI), which confirmed the production of a fluorescent conjugate for which the mean molecular weight (M_w) value was 14.6 kDa, and the number-average molecular weight (M_n) value was 7.8 kDa.

Additionally, differential scanning calorimetry experiment was performed for unmodified PLGA, PLGA-**5** conjugate and fluorophore **5**, Fig. S7–S9 (SI), showing obvious changes owing to incorporation of a fluorophore core into PLGA chains.

The degree of modification of the polymer carboxyl groups was determined spectrofluorometrically by measuring the amount of unlinked dye during extraction of the reaction mixture (Table S2, SI). Fig. S10 (SI) shows calibration curves for two types of fluorescent dyes, **1** and **5**. The degree of polymer substitution in all cases varied between 39–45%, enabling the production of nanoparticles with high spectral properties.

To verify the efficiency of covalent immobilization and quantify any unbound dye, the PLGA-**3** and PLGA-**5** conjugates – representing morpholine- and ethoxyethyl-substituted fluorophores, respectively – were analyzed by high-performance liquid chromatography (HPLC, Fig. S11–S14, SI). In both cases, the content of free dye in the final materials did not exceed 0.03%. This negligible quantity confirms nearly complete covalent attachment of the fluorophores and ensures that the measured photophysical and bioimaging properties of the PLGA–naphthalimide conjugates originate from stably bound species rather than free molecular dyes. The combination of synthetic precision and quantitative analysis thus validates the robustness of the covalent modification approach, establishing a reliable platform for subsequent fluorescence characterization and nanotechnological application.

The application of DFT for the prediction of the spectral luminescence properties of PLGA–naphthalimide 1–8 fluorescent polymers

A central element of this work involved applying density functional theory (DFT) to model PLGA-based polymers covalently modified with 1,8-naphthalimide derivatives and to predict their spectral-luminescent properties. These computational insights served as a foundation for the subsequent experimental synthesis of fluorescent nanoparticles designed for targeted drug delivery visualization. Given the relatively high molecular weight of commercial PLGA Resomer® RG 502 H (17 kDa), direct DFT treatment of the entire polymer chain is computationally impractical. Therefore, an approximation was adopted based on the hypothesis that the photophysical behavior of the PLGA–fluorophore conjugates is governed primarily by the electronic characteristics of the chromophore itself. In this context, the polymer backbone is expected to act mainly as an electronically inert scaffold that affects conformational freedom and the local environment rather than contributing to the frontier orbitals. This assumption is explicitly supported by the frontier orbital analysis (Fig. 2A and B): the HOMO and LUMO remain localized on the naphthalimide core, and attachment of a lactide–glycolide fragment does not introduce additional frontier states or appreciably alter the orbital shapes relevant to the lowest optically active transition. Therefore, extending the degree of polymerization is not expected to change the electronic character of the key excitation, while it would substantially increase conformational complexity. On this basis, subsequent electronic-structure simulations were performed on the naphthalimide derivatives themselves, while polymer attachment remains a structural/environmental factor, not included in the computational model.

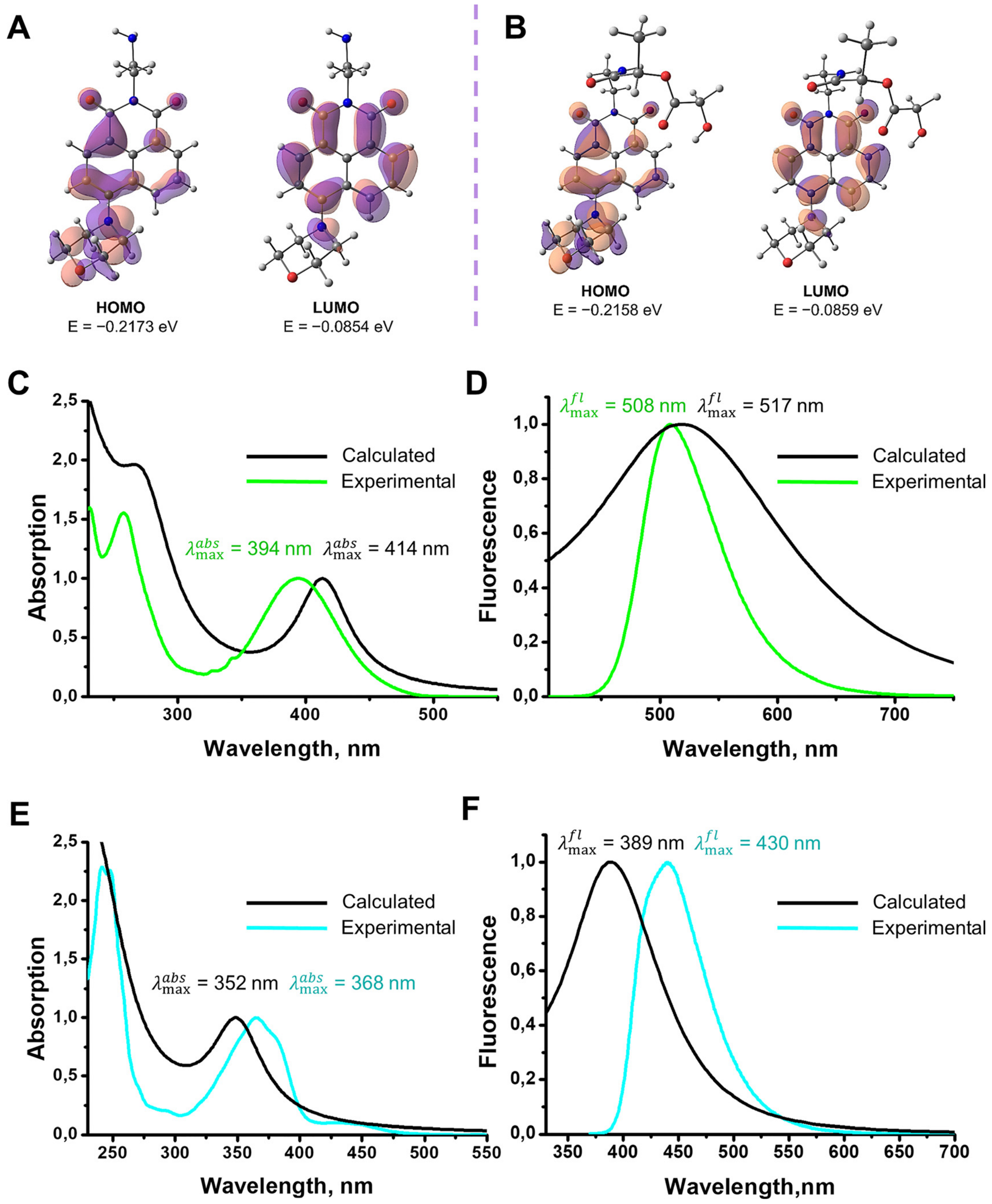

Fig. 2 (A) HOMO–LUMO orbitals and their energyes of the compound **1** computed at PBE0/def2-TZVP level of theory with dichloromethane as a solvent. (B) HOMO–LUMO orbitals and their energyes of the mono(lactide-glycolide)-fluorophore 1 computed at PBE0/def2-TZVP level of theory with dichloromethane as a solvent. (C) The experimental and TD-DFT calculated UV-Vis absorption spectra of the compound **1**. (D) The experimental and ESD calculated luminescence spectra of the compound **1**. (E) The experimental and TD-DFT calculated UV-Vis absorption spectra of the compound **5**. (F) The experimental and ESD calculated luminescence spectra of the compound **5**.

To further minimize computational cost during conformational searches, geometry optimization, and density functionals testing, compound **1** (dye **1**) was selected as the representative model, owing to its shortest carbon spacer between the naphthalimide core and the terminal amino group. This structural simplification reduced the number of atoms in the quantum system without compromising the validity of the photophysical predictions, since frontier orbitals analysis showed no contribution of carbon spacer and terminal amino group to HOMO and LUMO.

To enable direct comparison with experimental measurements, the absorption and fluorescence maxima were determined for both free fluorophore **1** and its PLGA-bound conjugate in dichloromethane. This solvent was chosen for its ability to dissolve both the dye and polymer, ensuring consistency in spectroscopic data generation. Polar aprotic solvents such as dichloromethane and DMSO are known to favor high extinction coefficients, quantum yields, and fluorescence brightness for 1,8-naphthalimide derivatives.

A functional screening of density functionals was performed to identify the most accurate methodology for predicting optical transitions in these naphthalimide systems, specifically the absorption maximum for compound **1**. The tested functionals included range-separated hybrid generalized-gradient-approximation (GGA) functionals (CAM-B3LYP, ωB97) and global-hybrid GGA functionals (PBE0, B3LYP), all combined with the def2-TZVP basis set. The theoretical absorption maxima were compared against the experimental value of 394 nm (Fig. S15, SI). The analysis revealed that global hybrids slightly overestimated the experimental wavelength, while range-separated hybrids tended to underestimate it. Among these, the PBE0/def2-TZVP level of theory provided the best overall agreement, particularly for naphthalimide chromophores whose transitions are predominantly local rather than strongly charge-transfer in nature. This observation is in line with prior literature reports confirming the suitability of the PBE0 functional combined with def2-TZVP basis set for predicting absorption spectra of comparable organic systems.[38]

Based on these results, the validated PBE0/def2-TZVP formalism was used to calculate the electronic structures and excited states of all synthesized derivatives **1–8**. The TD-DFT calculated absorption spectra successfully reproduced the main experimental features, notably the long wavelength absorption band at approximately 410 nm. To improve the comparison with experiment, the calculated stick spectra were convoluted with Lorentzian functions using a full width at half maximum (FWHM) of 16 nm (Fig. 2C).

Initial TD-DFT modelling of fluorescence spectra predicted emission maxima at 344 nm (for compound **1**) and 404 nm (for compound **5**), while experimental maxima were observed at 508 nm and 438 nm, respectively. Since these TD-DFT emission energies were evaluated from optimized S_1 geometries, the discrepancy does not arise from neglect of relaxation to the emissive excited-state minimum itself. Rather, it reflects the limitation of representing fluorescence by a single vertical electronic transition energy, whereas the experimentally observed fluorescence maximum corresponds to the maximum of a vibronically broadened emission band. This emphasizes the necessity of accounting for vibrational contributions to fluorescence in these naphthalimide systems.

Therefore, after selecting the electronic-structure level of theory from the absorption benchmark on compound **1**, we adopted a vibronic emission simulation using the ORCA excited state dynamics (ESD)[39] spectroscopy workflow, which allows to account for vibrational frequencies of different states *via* Franck–Condon (FC) mechanism. In contrast to a plain vertical TD-DFT emission energy, the ESD approach provides a vibronically structured band profile and is therefore more appropriate for direct comparison with experimentally observed fluorescence maxima. The rationale for a vibronic treatment is also supported by previously known results: Salikov *et al.* paper[38] demonstrated that inclusion of vibronic effects *via* a vertical Hessian Franck–Condon (VH|FC) approach improves agreement of absorption band maxima with experiment compared to relying on vertical TD-DFT energies alone. It is conceptually aligned with our choice of ESD module, albeit using adiabatic Hessian after a step (AHAS) instead of VH and predicting emission instead of absorption.

As a representative structural illustration, comparison of the optimized S_0 and S_1 geometries of dye **4** showed a noticeable difference between the two minima (RMSD = 0.812 Å), indicating non-negligible structural relaxation prior to emission.

Within ESD, Herzberg–Teller (HT) contributions were tested for compounds **1** and **5** and found to have a negligible effect on the position of the emission maximum. Consequently, all calculations for the full series of compounds **1–8** were performed without accounting for HT contributions to reduce computational cost.

Stated approach yielded emission maxima in good agreement with experiment, being 517 nm (for compound **1**, Fig. 2D) and 389 nm (for compound **5**, Fig. 2F). The UV-Vis absorption and photoluminescence spectra of the remaining derivatives (**2–4** and **6–8**) calculated *via* TD-DFT and ESD methods are presented in Fig. S16–S21 (SI), and the summarizing numerical data are compiled in Table 1.

Minor deviations for certain compounds, such as dye **4**, were attributed to the extended hydrocarbon substituent at the imide nitrogen, which can hinder geometry convergence and modify vibrational coupling. Similarly, larger discrepancies observed for derivatives **5–8** relative to **1–4** likely result from the increased conformational flexibility introduced by the ethoxyethyl substituent at the 4-position of the aromatic ring. Additionally, the use of implicit solvation models in these simulations limits the precision of excited-state conformational sampling, contributing to the observed variations.

Taken together, these results define a practical computational workflow for naphthalimide emitters under similar conditions (PBE0/def2-TZVP geometries and frequencies; TD-DFT for absorption; ESD(AHAS|FC) treatment for emission), which can be used as a starting point for predictive modelling and photophysical properties engineering of related 1,8-naphthalimide systems.

Table 1 Calculated and experimental maximum absorption and fluorescence wavelengths for dyes **1–8** in methylene chloride

	Absorbance wavelength maximum, λ_{max}^{abs}, nm			Fluorescence wavelength maximum, λ_{max}^{fl}, nm		
Fluorophore	TD-DFT	Experimental value	$\Delta\lambda_{max}^{abs}$,[a] nm	ESD	Experimental value	$\Delta\lambda_{max}^{fl}$,[b] nm
1	414	394	−20	517	508	−9
2	414	397	−17	520	512	−8
3	413	395	−18	517	510	−7
4	413	394	−19	538	508	−30
5	352	368	16	389	430	41
6	350	365	16	390	430	40
7	355	365	10	388	430	42
8	355	365	10	388	432	44

[a] $\lambda_{max}^{abs} = \lambda_{max\,Experimental}^{abs} - \lambda_{max\,TD\text{-}DFT}^{abs}$. [b] $\lambda_{max}^{fl} = \lambda_{max\,Experimental}^{fl} - \lambda_{max\,TD\text{-}DFT}^{fl}$.

This study also differs from known works in that it compares the efficiency of the TD-DFT and ESD approaches for predicting emission, the latter of which has been rarely used in theoretical descriptions of 1,8-naphthalimides.

Preparation of PLGA–1,8-naphthalimide 1–8 nanoparticles

Building on the preceding work, the synthesized PLGA–1,8-naphthalimide conjugates were employed as functional precursors for nanoparticle fabrication, enabling the development of fluorescent, traceable polymeric delivery systems. The formation of nanoparticles based on these conjugates establishes a direct link between molecular design and nanoscale performance, providing a foundation for constructing targeted carrier systems with intrinsic optical monitoring capability.

A wide range of physical and chemical strategies has been reported for PLGA nanoparticle preparation, including nanoprecipitation,[40] high-pressure homogenization,[41] microfluidic synthesis,[42] and ultrasonic dispersion.[43] Among these techniques, nanoprecipitation was selected for this study due to its simplicity, reproducibility, and ability to yield monodisperse nanoparticles of controlled dimensions under mild conditions. The method enables precise formation of particles with diameters below 120 nm – a size range widely considered optimal for passive tumor accumulation, endocytic uptake, and systemic circulation in biomedical applications.

The nanoprecipitation procedure was optimized to ensure reproducible particle formation. Nanoparticle synthesis was performed under the following conditions: (1) a 2% aqueous solution of poly(vinyl alcohol) (PVA) was used as the stabilizing phase; (2) acetone served as the organic phase, containing the PLGA–1,8-naphthalimide conjugate dissolved at a concentration of 5 mg mL^{-1}; and (3) the aqueous phase was stirred at 1500 rpm to promote uniform nucleation and controlled particle growth. The overall schematic of the synthetic route for PLGA–1,8-naphthalimide nanoparticles is presented in Fig. 3.

The obtained nanoparticles were systematically characterized in terms of hydrodynamic diameter, ζ-potential, and polydispersity index (PDI). The results, summarized in Table 2, demonstrate uniform size distribution and stable surface charge across all samples.

Importantly, the incorporation of fluorophores into the PLGA backbone did not significantly alter these physicochemical parameters, indicating that covalent linkage of the chromophore preserves the intrinsic self-assembly and colloidal stability of the polymer matrix. Such consistency confirms the robustness of the conjugation approach and supports the suitability of the resulting nanoparticles for subsequent optical studies and biological evaluation.

Investigation of the spectral properties of dyes, polymers and nanoparticles

Spectral properties of fluorophores 1–8. The photophysical behavior of the synthesized fluorophores **1–8** was comprehensively examined in three representative solvents – methylene chloride, dimethyl sulfoxide (DMSO), and water – to elucidate solvent-dependent changes in absorption and emission characteristics. The first series of compounds (**1–4**), bearing a morpholine substituent at the 4-position of the naphthalimide ring, displayed absorption maxima near 400 nm in aqueous media and intense fluorescence at approximately 530 nm, corresponding to the green region of the visible spectrum. The second group (**5–8**), containing an ethoxyethyl substituent at the 4-position of the aromatic nucleus, exhibited absorption maxima around 375 nm (in water) and emission peaks near 460 nm, placing their luminescence within the blue region. This clear spectroscopic distinction between substituent types

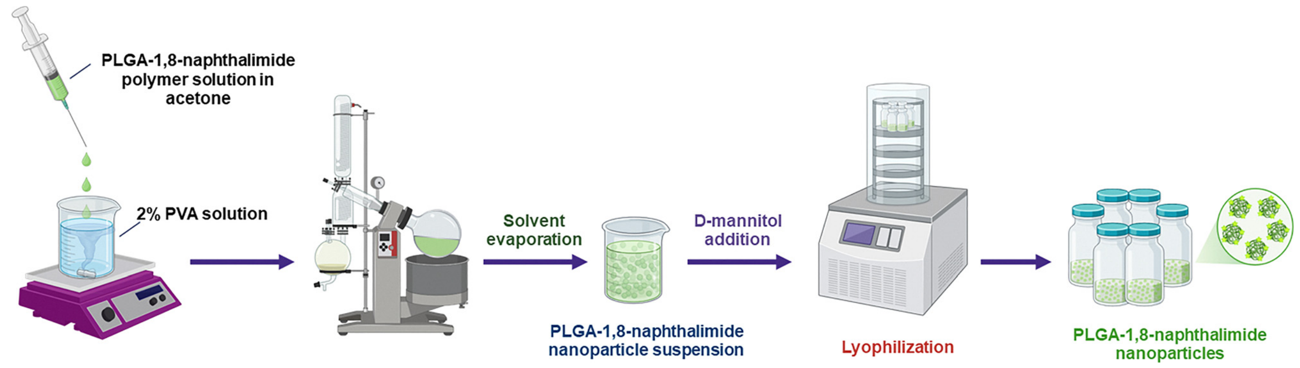

Fig. 3 General scheme for the synthesis of PLGA-1,8-naphthalimide nanoparticles.

Table 2 Properties of the obtained PLGA–naphthalimide **1–8** nanoparticles

PLGA–naphthalimide **1–8** nanoparticles	ξ-Potential, mV	Particle size, nm	PDI
PLGA-**1**	−13,8 ± 1.2	116.3 ± 2.3	0.146 ± 0.03
PLGA-**2**	−10.5 ± 1.0	89.4 ± 3.7	0.145 ± 0.01
PLGA-**3**	−15.3 ± 2.1	99.6 ± 5.2	0.117 ± 0.02
PLGA-**4**	−16.4 ± 1.1	125.8 ± 1.9	0.158 ± 0.02
PLGA-**5**	−15.9 ± 1.0	112.8 ± 6.1	0.193 ± 0.01
PLGA-**6**	−15.9 ± 1.2	109.2 ± 2.0	0.111 ± 0.01
PLGA-**7**	−11.4 ± 1.2	112.5 ± 1.7	0.132 ± 0.02
PLGA-**8**	−17.4 ± 1.3	108.9 ± 4.4	0.135 ± 0.03

highlights the strong influence of electron-donating groups on the naphthalimide π-system and validates the conceptual framework of substituent-controlled spectral tuning.

Within each group, the molecules differ by the length of the carbon spacer connecting the naphthalimide core to the terminal amino group. Experimental evaluation of these derivatives revealed no systematic dependence of spectral or luminescence properties on spacer length, implying that electronic transitions are primarily localized within the aromatic fragment rather than influenced by the distal chain. This phenomenon is consistent with an efficient intramolecular charge transfer (ICT) from the electron-donating substituent at the 4-position to the electron-accepting carboximide group. The nitrogen substituent at the imide position, by contrast, does not participate in this charge redistribution, as confirmed by DFT calculations.

All examined fluorophores exhibited a single narrow absorption band with pronounced mirror symmetry between the absorption and fluorescence spectra (Fig. S16–S28, SI). The parameters determined experimentally included absorption and emission maxima, molar extinction coefficients, fluorescence quantum yields, and overall fluorescence brightness in methylene chloride, DMSO, and water; all numerical data are provided in Table 3.

A particularly interesting observation concerns the morpholine-substituted derivatives **1–4**. Their fluorescence quantum yields in water were markedly reduced compared to those measured in organic solvents, with values around 1%. This pronounced quenching effect is attributed to the formation of a twisted intramolecular charge transfer (TICT) state, which arises from the rotational mobility of the 4-substituent in the excited state relative to the naphthalimide plane.[44,45] The resulting non-radiative relaxation processes dominate the excited-state decay, leading to diminished radiative deactivation and lowered quantum efficiency. It can reasonably be postulated that this non-emissive pathway will be suppressed in the solid state or within rigid polymeric environments, such as in PLGA-based nanoparticles, where restricted conformational freedom should restore higher fluorescence yields.

Quantitative analysis of the collected data revealed that, among the morpholine derivatives, compounds **3** and **4** (with four- and six-carbon spacers, respectively) exhibited the highest brightness values. In the ethoxyethyl-substituted series, the most promising fluorophores were identified as compounds **5** and **8**, containing two- and six-carbon linkers, respectively. These findings delineate a clear structure–property relationship within each derivative family, identifying optimal candidates for subsequent covalent immobilization and bioimaging applications within PLGA-based fluorescent nanomaterials.

Spectral properties of PLGA–naphthalimide polymers 1–8

At the next stage of the study, attention was directed toward understanding how covalent incorporation of the fluorophores into the PLGA matrix influences their spectral and luminescent properties. This assessment provides critical insight into the extent to which the local microenvironment of the polymer backbone modulates the photophysical behavior of attached chromophores. The absorption and fluorescence maxima, along with fluorescence quantum yields, were determined for all PLGA–naphthalimide conjugates in polar aprotic

Table 3 Spectral characteristics of naphthalimide derivatives **1–8** in methylene chloride, DMSO and water, 25 °C

	Fluorophore							
	1	**2**	**3**	**4**	**5**	**6**	**7**	**8**
Solvent – methylene chloride								
λ^{abs}, nm	394	397	395	394	368	365	365	365
λ^{fl}, nm	532	512	510	508	430	430	430	432
$\varepsilon \times 10^{-3}$, M^{-1} cm^{-1}	12.2	12.6	14.7	10.1	12.2	14.5	18.6	14.4
Fluorescence quantum yield, %	64.3	48.5	69.7	74.0	83.3	50.7	52.8	60.8
Brightness, M^{-1} cm^{-1}	7850	6110	10 250	7480	10 170	7350	9820	8760
Solvent – DMSO								
λ^{abs}, nm	400	402	402	401	368	357	368	368
λ^{fl}, nm	533	540	541	540	446	446	447	448
$\varepsilon \times 10^{-3}$, M^{-1} cm^{-1}	14.0	11.5	14.6	10.7	9.7	17.0	15.3	17.1
Fluorescence quantum yield, %	8.2	2.3	2.4	3.2	52.0	41.6	40.7	45.9
Brightness, M^{-1} cm^{-1}	1150	265	350	345	5040	7070	6230	8750
Solvent – water								
λ^{abs}, nm	400	403	401	400	375	373	375	374
λ^{fl}, nm	565	560	559	547	457	468	460	457
$\varepsilon \times 10^{-3}$, M^{-1} cm^{-1}	14.3	9.2	13.3	11.7	10.3	10.8	8.5	12.5
Fluorescence quantum yield, %	1.0	0.4	0.4	0.6	72.2	7.5	5.5	78.2
Brightness, M^{-1} cm^{-1}	143	37	53	70	7440	810	470	9780

Table 4 Spectral characteristics of the obtained polymers in methylene chloride and DMSO, 25 °C

	λ^{abs}, nm		λ^{fl}, nm		Fluorescence quantum yield, %	
Polymer	Methylene chloride	DMSO	Methylene chloride	DMSO	Methylene chloride	DMSO
PLGA-**1**	400	401	503	534	44.3	4.2
PLGA-**2**	399	401	515	539	63.7	2.9
PLGA-**3**	395	400	512	539	50.6	3.3
PLGA-**4**	393	398	508	540	67.9	3.7
PLGA-**5**	367	364	437	446	79.0	62.4
PLGA-**6**	366	369	429	445	49.3	42.5
PLGA-**7**	366	370	430	446	56.2	41.7
PLGA-**8**	364	367	431	447	60.1	43.9

Table 5 Spectral characteristics of the obtained nanoparticles PLGA–naphthalimide **1–8** in water, 25 °C

	λ^{abs}, nm	λ^{fl}, nm	Fluorescence quantum yield, %	Brightness of the sample, M^{-1} cm^{-1}
PLGA-**1**	400	507	15.6	5.272×10^{19}
PLGA-**2**	400	510	16.5	1.202×10^{20}
PLGA-**3**	394	508	24.5	1.347×10^{20}
PLGA-**4**	400	506	80.6	7.469×10^{20}
PLGA-**5**	365	451	54.4	1.067×10^{21}
PLGA-**6**	370	433	12.9	2.392×10^{20}
PLGA-**7**	375	436	5.1	7.076×10^{19}
PLGA-**8**	369	445	82.4	8.080×10^{20}

solvents – dichloromethane and DMSO. The obtained data are summarized in Table 4.

A key observation is that conjugation with PLGA does not fundamentally alter the electronic structure of the fluorophores. The main spectral features of the parent dyes are retained in the polymer conjugates, confirming that the covalent attachment does not lead to electronic perturbation of the naphthalimide chromophore. The resulting polymers display well-defined absorption and emission bands comparable in shape and intensity to those of the free fluorophores.

Nevertheless, the transition of naphthalimide units into the hydrophobic PLGA domain introduces subtle, yet reproducible, spectral shifts. Both absorption and fluorescence maxima exhibit minor shifts – on the order of up to 10 nm – depending on the specific fluorophore structure and solvent polarity. These shifts reflect microenvironmental effects associated with solvation and local dielectric changes near the fluorophore within the polymeric matrix. Importantly, these variations testify to the successful encapsulation of the emissive center in a less polar microenvironment created by the polymer backbone.

In DMSO, most polymer conjugates show a moderate increase in fluorescence quantum yield compared with their corresponding free fluorophores. This enhancement is indicative of restricted intramolecular mobility following covalent fixation, which reduces non-radiative decay pathways and stabilizes the excited state. The observed improvement in emission efficiency further confirms that PLGA serves not only as a structural carrier but also as a protective framework that reinforces optical stability of the conjugated fluorophores.

Overall, these results demonstrate that covalent integration of 1,8-naphthalimide derivatives into the PLGA matrix effectively preserves their photophysical properties while simultaneously enhancing emission performance under certain conditions. This outcome is particularly promising for the creation of robust fluorescent polymeric materials, where long-term stability, solvent tolerance, and retention of brightness are critical for reliable tracking and bioimaging applications.

Spectral properties of PLGA–naphthalimide 1–8 nanoparticles

The spectral analyses of the PLGA–naphthalimide nanoparticles revealed a set of distinct optical trends reflecting the successful incorporation of the fluorophore units into the polymer matrix (Table 5).

The absorption spectra of the nanoparticles display broad, featureless profiles predominantly dominated by PLGA scattering and matrix absorption, with only a weakly resolved band corresponding to the fluorophore fragment. This observation is expected given the low dye content within the polymer backbone and the resulting dilution of the chromophoric component relative to the polymer mass. Despite this, the fluorescence spectra exhibit well defined emission bands corresponding closely to those of the parent fluorophores, confirming that the intrinsic emissive characteristics are retained following nanoparticle formation.

A slight broadening and small spectral shift of the fluorescence bands were consistently observed compared with the free dyes and their polymer conjugates (Fig. 4). These changes are indicative of altered microenvironments experienced by the fluorophores upon transition to the nanoparticle state. Specifically, the increased heterogeneity within the polymeric domain and the presence of local polarity gradients within the nanoparticle cores likely contribute to the modest spectral displacement and line broadening. Such behavior is common for fluorophores incorporated into complex macromolecular assemblies where partial restriction of chromophore motion and microenvironmental variation subtly modulate emissive behavior.

Analysis of the spectral-luminescent data identified compounds **4**, **5**, and **8** as the most promising candidates for further study. Nanoparticles based on these fluorophores demonstrated the brightest emission and the highest photostability under comparable conditions. Notably, the brightness values of these nanoparticles exceeded those typical of standard PLGA-based systems functionalized with conventional dyes such as cyanines by one to two orders of magnitude. This substantial enhancement underscores the efficiency of the 1,8-naphthalimide framework and its compatibility with the PLGA environment for generating highly emissive, stable fluorescent nanomaterials.

A comparative summary of the spectral characteristics of individual dyes, corresponding polymer conjugates, and the resulting nanoparticles is provided in Table S3 (SI). The data clearly demonstrate that the optical performance of the newly developed PLGA–naphthalimide nanoparticles substantially

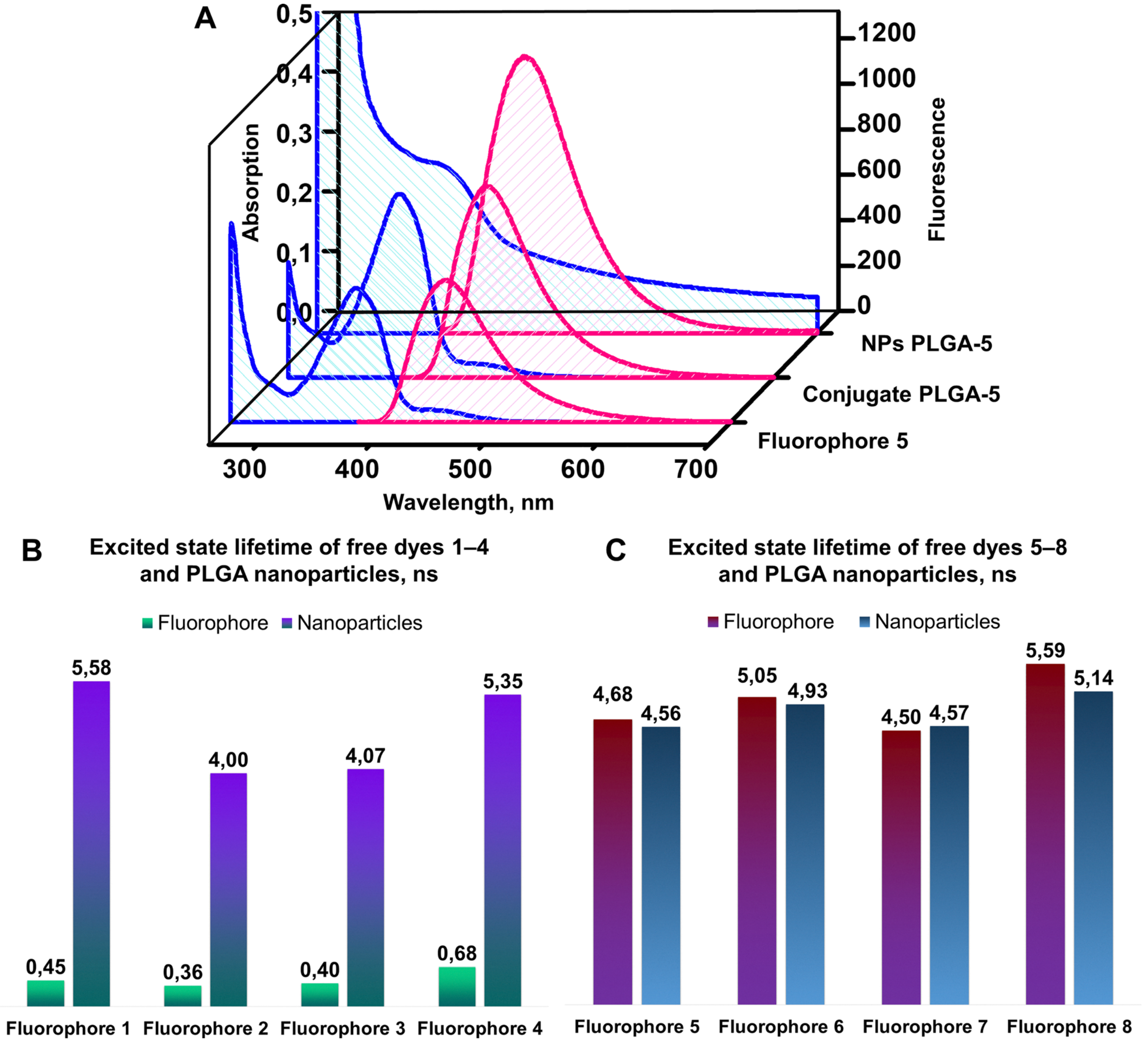

Fig. 4 (A) Absorption and fluorescence spectra of fluorophore 5 in DMSO (concentration [5] – 17 μg mL^{-1}), PLGA-5 conjugate in DMSO (concentration [PLGA-5] – 10.0 mg mL^{-1}) and PLGA-5 nanoparticles in water (concentration [NPs PLGA-5] – 2.5 mg mL^{-1}). (B) Average lifetimes of excited states of fluorophores 1–4 in free form and in nanoparticles. (C) Average lifetimes of excited states of fluorophores 5–8 in free form and in nanoparticles.

surpasses that of widely used fluorescent markers employed in PLGA modification protocols. These findings highlight the potential of the synthesized systems as advanced tools for optical bioimaging, theranostics, and real-time nanoscale visualization applications.

Investigation of the fluorescence lifetimes of fluorophores in the free form and as part of nanoparticles

To gain deeper insight into the mechanisms underlying the variation of fluorescence quantum yields in different media, an additional series of experiments was conducted to measure the fluorescence lifetimes of the fluorophores in their free molecular form and when incorporated into PLGA-based nanoparticles. Time-resolved measurements were performed using fluorescence lifetime imaging microscopy (FLIM), which provides quantitative information on excited-state dynamics with spatial resolution.[46] Representative FLIM micrographs and analytical data are presented in Fig. 4(B, C) and Table S4 (SI).

Excitation of the samples was achieved with a femtosecond pulsed laser operating at 770 nm, enabling efficient two-photon excitation of the fluorophore chromophores. Time-correlated single photon counting (TCSPC) analysis was employed to derive the decay profiles and calculate the mean fluorescence lifetimes τ_{mean} for each sample.

The results reveal a pronounced difference between the free fluorophores and those embedded within nanoparticles. For the morpholine-substituted derivatives **1–4**, the average excited-state lifetime in solution was found to be on the order of 0.5 ns, whereas incorporation into PLGA nanoparticles led to a substantial increase to 4–5 ns. This approximately tenfold enhancement in lifetime strongly supports the hypothesis that molecular fixation within the rigid polymer matrix suppresses non-radiative deactivation pathways associated with the formation of the twisted intramolecular charge transfer (TICT) state. In the free state, the conformational flexibility of the 4-position substituent allows rotation in the excited state, promoting TICT-type quenching and shortening the observed lifetime. Upon immobilization within the nanoparticle core, these intramolecular rotations are effectively restricted, resulting in stabilization of the emissive state and prolongation of fluorescence decay times.

The observed correlation between fluorescence lifetime extension and the quantum yield enhancement previously noted for the same systems confirms that structural confinement within the PLGA matrix effectively mitigates TICT-driven non-radiative losses. These results emphasize that the incorporation of fluorophores into a well-defined polymeric microenvironment not only preserves fluorescence intensity but also governs the excited-state relaxation mechanisms, providing a molecular basis for the exceptional brightness and stability of PLGA–naphthalimide nanoparticles in bioimaging applications.

Recent work by Dai *et al.*[22,35] has expanded the utility of 1,8-naphthalimide scaffolds in microenvironment-responsive sensing demonstrating TICT-based viscosity detection in cells and liquid foods[22] and ICT/TICT-switchable ''turn-on'' water sensing in organic media.[35] In contrast to these small-molecule probes whose emission relies on solvent-dependent conformational dynamics, our PLGA–naphthalimide nanoparticles achieve constitutive fluorescence enhancement through matrix-imposed chromophore immobilization, thereby suppressing non-radiative decay pathways independent of local polarity or viscosity fluctuations and ensuring robust signal output across diverse biological environments.

Stability investigation of PLGA–naphthalimide 1–8 nanoparticles

Prior to conducting fluorescence imaging experiments, it was essential to evaluate the colloidal and optical stability of the synthesized PLGA–naphthalimide nanoparticles under physiologically relevant conditions. Stability assays were performed in phosphate-buffered saline (PBS), RPMI-1640, and DMEM media at 37 °C using nanoparticles derived from two representative conjugates: PLGA-4 (morpholine substituent) and PLGA-**8** (ethoxyethyl substituent). Samples were collected after 1, 2, 3, 4, 5, 6, 24, and 48 hours. The hydrodynamic diameter of the nanoparticles was determined by dynamic light scattering (DLS), while fluorescence intensity was monitored to assess optical stability. The complete results are summarized in Tables S5 and S6 (SI).

The obtained data indicate that the nanoparticles maintain high physical stability within the first six hours, showing only minimal variation in size. In all measurements, the polydispersity index (PDI) remained below 0.2, confirming the formation of monodisperse systems within acceptable limits for biomedical use. Over extended incubation periods, moderate aggregation was observed, most prominently in RPMI-1640 after 48 hours, likely due to protein components and ionic strength effects inherent to this medium (Fig. S47–S49 and Table S5 SI).

The temporal evolution of fluorescence intensity followed a hyperbolic decay for PLGA-**4** nanoparticles in all tested environments (Fig. S50, SI), suggesting partial quenching or gradual structural rearrangement of the morpholine-substituted fluorophores. In contrast, PLGA-**8** nanoparticles exhibited stable fluorescence with only minor signal fluctuations across the entire 48 hour interval (Fig. S51, SI), reflecting improved resistance to environmental quenching effects.

Overall, the findings demonstrate that PLGA–naphthalimide nanoparticles possess adequate physical and optical stability in PBS, RPMI-1640, and DMEM media under physiological temperature conditions. Aggregation is negligible up to at least 24 hours, and fluorescence remains largely preserved – particularly for systems based on the ethoxyethyl-substituted fluorophore – affirming their suitability for time-resolved imaging and *in vitro* biological studies.

Quantitative cytotoxicity assessment of PLGA nanoparticles

To provide quantitative support for the biocompatibility claims and establish a defined biosafety window for cellular imaging applications, resazurin reduction assays (Alamar Blue®) were conducted on representative PLGA–naphthalimide nanoparticles. Fig. S52 (SI) shows the viability results for PLGA-**5** nanoparticles tested across a concentration range of 50–400 μg mL^{-1} on 4T1 mouse mammary carcinoma cells following 24 h exposure. Cell viability remained consistently above 95% throughout the entire concentration range, confirming excellent cytocompatibility at doses relevant for fluorescence microscopy and live-cell tracking experiments.[47–49]

These data delineate a clear operational window for *in vitro* applications and complement the qualitative morphological observations previously reported. Experimental details, including cell seeding density, incubation conditions, and fluorescence readout parameters (λ_{ex} = 535 nm, λ_{em} = 620 nm), are provided in the Materials and methods section.

In vitro bioimaging of nanoparticles on 4T1 cell line

To assess the cellular uptake and intracellular localization of the most promising fluorescent systems, *in vitro* bioimaging studies were carried out using live 4T1 mouse mammary carcinoma cells. Nanoparticles based on fluorophores **4** and **5** were selected for this investigation owing to their favorable brightness and photostability. Lysosomes were selectively stained with LysoTracker Red DND-99 dye (50 nM), which accumulates in acidic cellular organelles and thereby provides a reliable marker for endocytic and lysosomal compartments.

Following dye staining, the nanoparticle suspensions were introduced into the cell culture medium and incubated under physiological conditions. After incubation, the cells were rinsed with phosphate-buffered saline to remove unbound nanoparticles. Real-time confocal laser scanning microscopy was performed using a Nikon A1R MP inverted microscope with laser lines of 405 nm and detection windows of 500–550 and 425–475 nm for PLGA-**4** and PLGA-**5**, respectively. Representative fluorescence micrographs depicting intracellular distribution of

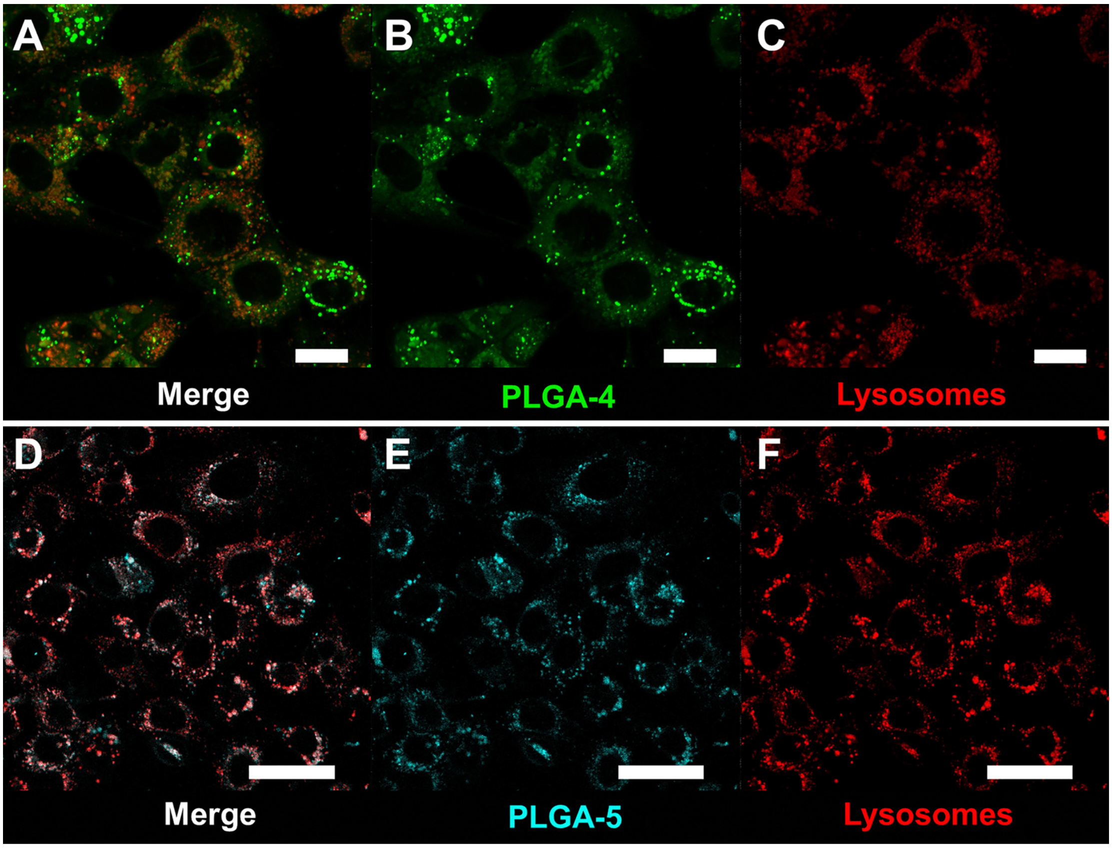

Fig. 5 (A)–(C) Confocal imaging of 4T1 cells after incubation with PLGA nanoparticles labelled with fluorophore 4: A – merged image; B – 30 minutes after incubation with NPs PLGA-4; C – cell lysosomes stained with LysoTracker Red DND-99 (red). Scale bar – 20 μm. (D)–(F) Confocal imaging of 4T1 cells after incubation with PLGA nanoparticles labelled with fluorophore 5: A – merged image; B – 30 minutes after incubation with NPs PLGA-5; C – cell lysosomes stained with LysoTracker Red DND-99 (red). Scale bar – 50 μm.

PLGA-**4** and PLGA-**5** nanoparticles after 30 minutes of incubation are presented in Fig. 5(A–C) and (D–F), respectively.

The imaging data confirmed strong intracellular fluorescence and well-defined nanoparticle localization within the cytoplasmic space, with no adverse effects on cellular morphology or viability. Quantitative analysis of the fluorescence signal colocalization between nanoparticles and lysosomes was performed using Pearson's correlation coefficient (PCC) and Manders' overlap coefficient (MOC). These parameters serve as quantitative indicators of organelle-specific accumulation and entry pathways. For PLGA-**4** nanoparticles, the PCC and MOC values were 0.68 and 0.72, respectively; for PLGA-**5**, 0.63 and 0.70. These high correlation values demonstrate a strong degree of colocalization with lysosomal compartments, consistent with internalization through a clathrin-mediated endocytosis pathway.

The confirmed lysosomal accumulation underscores that these nanoparticles undergo controlled intracellular trafficking typical of endosomal–lysosomal pathways, which is crucial for the design of therapeutic carriers directed toward intracellular targets. The absence of cytotoxic effects, combined with stable fluorescence and high imaging contrast, highlights the potential of PLGA-naphthalimide nanoparticles as versatile tools for cell-tracking, targeted delivery, and mechanistic exploration of lysosome-associated disorders and nanomedicinal systems.

In vitro bioimaging of nanoparticles on the transfected HeLa cell line

Despite the widespread use of commercially available markers that selectively bind to organelles, fluorescent proteins offer significant advantages in the highly specific labeling of cellular structural elements. Therefore, we decided to visualize the distribution of PLGA-**4** nanoparticles on the transfected HeLa cell line *in vitro*. For this purpose, cells were transfected with plasmids encoding LAMP1-mScarlet or mKate2-clathrin under CMV promoter and SV40 terminator control. The LAMP1-mScarlet fusion protein was used to visualize lysosomal compartments of cells, while visualization of clathrin using the mKate2-clathrin protein can provide information on the uptake of PLGA particles by living cells. Thus, the far-red protein mKate2 has an excitation maximum at 588 nm and an emission maximum at 633 nm, while the mScarlet protein has excitation and emission maxima at 569 and 594 nm, respectively.[50] This allows the fluorescence channels of the studied PLGA-**4** nanoparticles and fusion proteins to be separated using an ONI Nanoimager super-resolution microscope. The experiment was performed for 30 minutes after incubation with 200 μg mL^{-1} of

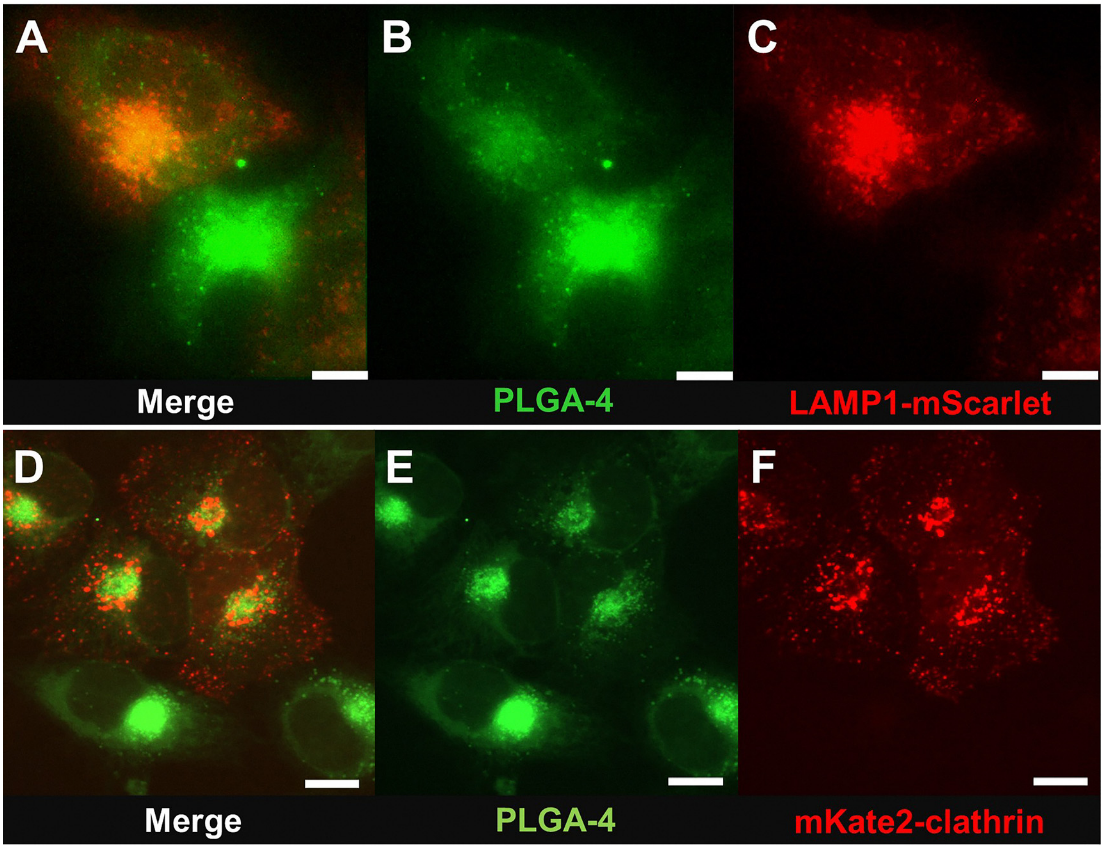

Fig. 6 (A)–(C) Live cell visualisation of the HeLa cell line after incubation with PLGA-4 nanoparticles: A – merged image; B – 30 minutes after incubation with 200 μg mL^{-1} of NPs PLGA-4; C – image of the transmembrane protein LAMP1-mScarlet. (D)–(F) Live cell visualisation of the HeLa cell line after incubation with PLGA-4 nanoparticles: A – merged image; B – 30 minutes after incubation with 200 μg mL^{-1} of NPs PLGA-4; C – image of mKate2-clathrin fluorescent protein. Images were acquired using a Nanoimager S microscope with 405 nm and 561 nm laser excitation. First images of a representative series are shown. Scale bar – 5 μm.

PLGA-4 nanoparticle suspension. Fluorescence images of the PLGA-**4** nanoparticle distribution on two transfected HeLa cell lines are shown in the Fig. 6(A–F).

Distinct spatial patterns were observed in comparison to earlier experiments on 4T1 carcinoma cells. In cells expressing mKate2-clathrin, the nanoparticles displayed partial localization near the endoplasmic reticulum but also co-localized with distinct clathrin-associated structures, confirming that clathrin-mediated endocytosis remains the dominant uptake pathway for PLGA nanoparticles in mammalian cells.[51] In cells expressing LAMP1-mScarlet, the PLGA-**4** nanoparticles predominantly accumulated in acidic organelles corresponding to lysosomal compartments, in agreement with the results obtained for the 4T1 cell line.

Together, these findings provide the first demonstration of intracellular trafficking and compartmentalization of PLGA nanoparticles covalently labeled with 1,8-naphthalimide fluorophores both in cells stained with conventional organelle-specific dyes and in transfected cells expressing targeted fusion proteins. The high fluorescence intensity, spectral stability, and resistance to photobleaching of the incorporated fluorophore confirm the potential of these materials as reliable tools for live-cell imaging. The developed PLGA–naphthalimide nanoparticles thus represent a robust platform for designing fluorescent targeted delivery systems and advanced nanoscale formulations, with significant prospects for studying intracellular processes and developing therapeutic strategies for diseases linked to lysosomal dysfunction and endocytic regulation.

Photostability investigation of PLGA–naphthalimide nanoparticles

Photostability represents a critical performance parameter for fluorescent nanoparticles, as sustained emission under continuous illumination is essential for reliable bioimaging. Traditional dyes such as fluorescein isothiocyanate (FITC) and Alexa Fluor 568 exhibit well-documented photobleaching limitations that restrict their nanotechnological utility.[52] Given the established photostability advantage of 1,8-naphthalimide derivatives,[53] we evaluated our systems through complementary benchmarking approaches considering experimental accessibility and resource constraints.

Relative stability *vs.* PLGA–Cy5 under biological imaging conditions

We initially compared PLGA–naphthalimide **5** nanoparticles with PLGA–Cy5 – a widely used commercial benchmark – under standard live-cell microscopy settings. Samples were normalized by percentage of maximum laser power and identical acquisition parameters, enabling relative photostability assessment representative of routine biological experiments (405 nm for naphthalimide 5; 637 nm for Cy5; ~4.7 mW cm^{-2} for lasers in both cases respectively). Fig. S53 (SI) shows normalized intensity decay over 7 min continuous exposure in 4T1 cells. PLGA-**5** reached 50% intensity after 3.5 min ($t_{1/2}$ = 3.5 min), while PLGA-Cy5 photobleached twice as rapidly ($t_{1/2}$ = 1.7 min). This ~2-fold advantage under practical, non-optimized conditions confirms operational stability suitable for extended cellular tracking.

Controlled single-wavelength study: matrix protection effects

Given resource considerations and experimental feasibility, we conducted a complementary assessment under uniform 405 nm excitation (9 min, ~4.7 mW cm^{-2}) comparing: (i) free fluorophore 4-stained fixed cells (30 min post-incubation/staining); (ii) PLGA-**4** nanoparticles-stained fixed cells (30 min post-incubation/staining); and (iii) DAPI-stained fixed cells (30 min post-incubation/staining; DAPI per Sigma-Aldrich protocol). The cells were fixed with 4% formaldehyde solution in PBS. Fig. S54 (SI) reveals free fluorophore 4 decayed ~66%, while PLGA-encapsulated dye lost only 8% – ~9× stabilization attributable to the polymer matrix shielding the chromophore from photooxidative damage. DAPI remained virtually unchanged, exhibiting slight enhancement characteristic of fixed cells where photoactivation and DNA concentration effects amplify signal.[54,55]

These orthogonal assessments – relative benchmarking (*vs.* Cy5) and controlled matrix study (*vs.* free dye/DAPI) – collectively validate naphthalimide photostability. The protective encapsulation effect enables prolonged, high-fidelity imaging, distinguishing this platform for longitudinal nanoparticle tracking.

We performed a pilot comparison under identical excitation conditions (~4.7 mW cm^{-2} for lasers in both cases respectively) with a commercially available dye (Cy5) commonly used in drug delivery research. This side-by-side assessment was designed to demonstrate that our new naphthalimide label performs adequately for *in vitro* visualization and intracellular distribution studies under the conditions tested. We note that this comparison does not imply general superiority across all imaging modalities or biological contexts.

The protective encapsulation effect enables prolonged, high-fidelity imaging, distinguishing this platform for longitudinal nanoparticle tracking *in vitro*. Future work will involve systematic benchmarking against commercial fluorophores for *in vivo* imaging applications.

Conclusions

This study demonstrates an integrated computational–experimental strategy for the rational design of fluorescent polymeric nanomaterials for *in vitro* cellular imaging applications. Time-dependent density functional theory (TD-DFT) calculations on isolated fluorophores, when combined with vibronic band simulations, provided a semi-quantitative description of the photophysical properties of PLGA conjugates, confirming the electronically passive role of the polymer matrix and validating a computationally efficient design approach. Guided by these insights, PLGA nanoparticles functionalized with 1,8-naphthalimide derivatives were synthesized and exhibited fluorescence intensities markedly enhanced – by up to two orders of magnitude under the specific imaging conditions employed in this work – relative to conventional dye-encapsulated systems, while retaining excellent photostability, colloidal stability, and biocompatibility in cell culture media. Fluorescence lifetime imaging microscopy (FLIM) revealed suppressed non-radiative decay resulting from restricted chromophore mobility within the polymer matrix, providing a molecular basis for the enhanced quantum yield and prolonged excited-state lifetime. *In vitro* studies confirmed efficient cellular internalization *via* clathrin-mediated endocytosis and predominant lysosomal localization in 4T1 and HeLa cell lines. Collectively, this work establishes a generalizable framework for engineering bright, photostable polymeric nanoprobes with precisely tunable optical properties, demonstrating their utility for high-fidelity intracellular imaging. Extension to *in vivo* theranostic applications will require further comparative benchmarking against established imaging agents under physiologically relevant conditions.

Experimental methods

Materials and instrumentation

The 1,8-naphthalimide derivatives **1–8** discussed in this work were obtained using the methods we developed earlier and presented in work.[37] Poly(lactic-*co*-glycolic acid) PLGA (Resomer® RG 502 H, Lot No. 170300516, Evonik Röhm GmbH, Germany) was used as the base polymer. *N*-Hydroxysuccinimide (Sigma-Aldrich, Germany), 1-ethyl-3-(3-dimethylaminopropyl)-carbodiimide, diisopropylethylamine (DIPEA), poly(vinyl alcohol) (9–10 kDa, 80% hydrolysed, Sigma-Aldrich, Germany), and D-mannitol (Dia-M, Russia) were used as received. Coumarin-6 and quinine sulfate (Sigma-Aldrich, USA) served as reference dyes for quantum yield measurements. Resazurin was manufactured by Cayman, USA. DAPI was manufactured by Sigma-Aldrich, USA. Deionized water was used in all experiments. Organic solvents (Aldrich, Merck, Alfa Aesar, EKOS-1) were used without further purification unless otherwise stated. Solvents from Aldrich and Acros with spectroscopic purity were used for the recording of absorption and fluorescence spectra.

The 4T1 mouse mammary carcinoma cell line was obtained from ATCC® (Cat. No. CRL-2539).

Microfiltration was performed using Millipore nylon membranes with a 0.045 μm pore size.

Thin-layer chromatography (TLC) was carried out on DC-Alufolien Kieselgel 60 F254 silica plates. Magnetic stirring was conducted using an RT 10 stirrer (IKA-Werke GmbH & Co. KG, Germany), and solvent evaporation was performed on a

Hei-VAP Core rotary evaporator (Heidolph Instruments GmbH & Co. KG, Germany).

^{1}H and ^{13}C NMR spectra were recorded on Bruker Avance spectrometers operating at 400 MHz, using tetramethylsilane as the internal standard. Samples were collected in deuterated $CDCl_3$ solvent. Chemical shifts were measured to the nearest 0.01 ppm, and coupling constants were measured to the nearest 0.1 Hz.

Nicolet 380 FTIR spectrometer (Thermo Fisher Scientific Inc., USA) with an ATR attachment and additional equipment.

A high-pressure waters chromatograph equipped with a Rheodyne 7161 injector, a Styrogel HR 4E + 5E column system, Milton Roy UV Spectromonitor 3100 detectors, a Waters RI 2414 refractometer, and Z-lab data acquisition and processing software was used. The system was calibrated using a set of waters polystyrene standards with an M_w of 600–500 000.

Differential scanning calorimetry was performed using a DSC 204 F1 Phoenix (Netzsch, Germany). The study was conducted over a temperature range of −100 to 150 °C in an inert gas flow (argon) of 60 mL min^{-1} with a heating rate of 10 °C min^{-1}.

High-performance liquid chromatography (HPLC) analyses were performed on a Millichrom A-02 chromatograph equipped with a UV detector and a ProntoSIL-120-5-C18 column (2 × 75 mm, 5 μm). Gradient elution was carried out using the following mobile phases: eluent A, a 0.2 M aqueous $LiClO_4$ solution with 0.05 M $HClO_4$, and eluent B, acetonitrile.

Nanoparticle size and ζ-potential measurements were performed by dynamic light scattering (DLS) using a Nano ZS Zetasizer system (Malvern Panalytical Ltd, UK), calibrated daily using manufacturer-recommended polystyrene standards (40 nm, 80 nm, 150 nm, and 200 nm latex spheres).

Electronic absorption spectra were obtained with a UV-1800 scanning spectrophotometer (Shimadzu, Japan), and fluorescence spectra were recorded using an RF-6000 spectrofluorometer (Shimadzu, Japan) at 25 ± 1 °C. The fluorescence signal was collected at 90° to the excitation beam, and spectra were corrected for photomultiplier sensitivity.

Fluorescence lifetime measurements were carried out using a FLIM module (Becker & Hickl, Germany) coupled to an LSM-710-NLO laser-scanning microscope (Carl Zeiss, Germany). Excitation was performed with a Chameleon Ultra II femtosecond laser (Coherent, USA; pulse width 140 fs, repetition rate 80 MHz, λ = 770 nm). The FLIM setup included a TCSPC system (SPC-150), hybrid GaAsP HPM-100-07 detector, and SPCImage 8.0 software (Becker & Hickl, Germany) for data acquisition and decay analysis.

Real-time confocal imaging was performed using a Nikon A1R MP inverted microscope (Nikon, Japan) equipped with a 405 nm laser (emission 410–470 nm). Maximum intensity projections along the *Z*-axis were generated with NIS-Elements AR software.

Live-cell images for Fig. 6 was acquired with Nanoimager S (ONI, UK) equipped with UPlanSApo 100 × 1.4NA oil immersion lens (Olympus), 488 nm and 640 nm lasers, 560 nm dichroic mirror and Scope8 sCMOS camera. Images were captured in TIRF regime using 405 nm laser for PLGA-4 nanoparticles excitation ($\approx$157.5 W cm^{-2}) and 561 nm laser for mScarlet or mKate2 excitation ($\approx$157.5 W cm^{-2}). A series of multiple images (up to 7500 frames) were obtained at 33 fps with 1405 nm excitation frame followed by 1561 nm excitation frame. Image acquisition was performed using NimOS 1.7.3.10248. Image processing was performed using NimOS 1.7.3.10248 and ImageJ FiJi ver. 1.53q. Image reconstruction was performed using default parameters of initial sigma.

Computational details

Conformational search and Geometry optimization. The conformational search was conducted using the CREST package version 2.12,[56] employing the GFN2-xTB method[57] with ALPB solvation model[58] with dichloromethane as the solvent. The resulting conformational ensemble was sorted by energy, and the lowest-energy conformers were selected for subsequent DFT calculations.

All DFT calculations were performed using the ORCA 5.0.4 quantum chemistry program package.[59] Geometry optimizations and frequency calculations were carried out using the PBE0 hybrid functional[60] in conjunction with the def2-TZVP basis set. The absence of imaginary frequencies was confirmed through vibrational frequency analysis, indicating true minima on the potential energy surface. To account for dispersion interactions, Grimme's D4 dispersion correction was applied.[61] Solvent effects were incorporated using the conductor-like polarizable continuum model (CPCM) with dichloromethane (CH_2Cl_2) as the solvent. All calculations employed tight optimization (TIGHTOPT) and self-consistent field (TIGHTSCF) convergence criteria to ensure high-accuracy results.

The UV-Vis absorption spectra were computed using time-dependent DFT (TD-DFT), including 30 singlet electronic states, with dichloromethane (CH_2Cl_2), consistent with experimental conditions. Several exchange–correlation functionals were evaluated to achieve accurate spectral predictions, including range-separated hybrids (CAM-B3LYP, ωB97X) and global-hybrid GGAs (B3LYP, PBE0). The PBE0/def2-TZVP combination provided the best agreement with experimental data.

To calculate the fluorescence spectra, structures were optimized to the first singlet excited state (S_1), including 8 singlet electronic states, using TD-DFT/PBE0/def2-TZVP level of theory, with subsequent calculation of their Hessian matrix. After that, calculation of absorption spectra on first excited state starting geometry, which corresponds to calculation of fluorescence spectra, was conducted to obtain plain TD-DFT results for emission.

Calculations *via* the ESD module were conducted in combination with TD-DFT formalism using adiabatic Hessian after a step (AHAS) approach, accounting for S_0 and S_1 vibrational frequencies. Herzberg–Teller contribution test for compound **1** was done *via* setting parameter "DOHT" to "TRUE". Voigt lineshape, spectral resolution (SPECRES) = 10, spectral width (LINEW) = 2500 cm^{-1}, and scaling parameter 0.9944 for PBE0/def2-TZVP combination[62] were used for all final ESD calculations.

Detailed computational details are provided in the SI.

Synthesis of PLGA-1–PLGA-8 conjugates

The dye (10 g, 1 equiv.) was dissolved in 1 mL of methylene chloride, and the PLGA polymer (Resomer® RG 502 H) (500 g) was dissolved in 3 mL of methylene chloride. Furthermore, 1-ethyl-3-(3-dimethylaminopropyl)carbodiimide (EDC, 10 equiv.) and *N*-hydroxysuccinimide (NHS, 10 equiv.) were dissolved in 3 mL of methylene chloride each. The EDC solution was added sequentially to the flask containing the polymer, followed by the NHS solution. A quantity of 25 μL of DIPEA was then added to the reaction mixture. Following a period of four hours, a dye solution in methylene chloride was introduced. The reaction mixture was stirred for 48 hours at room temperature. The resulting solution was extracted with a mixture of 10 mL of methylene chloride and 10 mL of distilled water (twice), 10 mL of distilled water and 10 mL of methanol (once), and 25 mL of distilled water (twice) to remove water-soluble by-products and starting reagents. The organic phase was separated, dried over anhydrous sodium sulphate, and then evaporated on a rotary evaporator at a rotor speed of 100 rpm and a temperature of T = 40 °C. The resulting precipitate was dissolved in 5 mL of ethyl acetate, following which the solution was added to 50 mL of hexane in order to precipitate the polymer. The resultant precipitate was then filtered and dried in air. The formation of the conjugate was determined by thin-layer chromatography (eluent : dichloromethane : methanol : water, 6.5 : 2.5 : 0.4).

Synthesis of PLGA-1–PLGA-8 nanoparticles

Polymer samples (10 mg) were dissolved in 2 mL of acetone. The resulting solution was then injected with a syringe into 10 mL of a 2% solution of polyvinyl alcohol, with the solution being subjected to intensive stirring (1500 rpm). The acetone was then removed on a rotary evaporator at a rotor speed of 100 rpm and a temperature of T = 40 °C. The analysis of the particle sizes was conducted by means of laser dynamic light scattering. A cryoprotectant (D-mannitol) was added to the nanoparticle suspension in an amount necessary to achieve a concentration of 2.5 wt%. The suspension was then poured into penicillin vials in 1 or 2 mL portions, frozen at −70 °C and lyophilised in two stages: the first stage – primary drying – 20 hours at a pressure of 0.30 mbar, the second stage – final drying – 4 hours at a pressure of 0.12 mbar.

Calibration curve for determining the residual content of dye 3 in the polymer and nanoparticles

In order to ascertain the residual dye **3** content in the polymer, five calibration solutions with concentrations ranging from 0.011 to 0.172 mg mL^{-1} were prepared. The dye was dissolved in acetonitrile. Gradient elution was employed, transitioning from 5% eluent B to 95% eluent B, with a volume of eluent passing through the column measuring 2500 μL. The wavelength of the UV detector was 230 nm. The time constant was determined to be 0.18 seconds. The volume of the sample applied to the chromatographic column was 2 microlitres. Following the analysis, the peaks obtained were processed using the MultiChrom programme. Consequently, a calibration curve of dye concentration (mg mL^{-1}) *versus* absorbance was obtained, with a correlation coefficient of R = 0.9991, described by the equation $Q = 0.03456 \times A$. The elution time of the dye was found to be 9.04 minutes.

Calibration curve for determining the residual content of dye 5 in the polymer and nanoparticles

The calibration curve for dye **5** was determined through the preparation of six solutions, ranging from 0.007 to 0.236 mg mL^{-1}. The solvent used was acetonitrile. Eluent B was acetonitrile. Gradient elution was employed, whereby the eluent was transitioned from 5% eluent B to 95% eluent B. The volume of eluent that passed through the column was 2500 μL. The wavelength of the UV detector was 240 nm. The time constant was determined to be 0.18 seconds. The volume of the sample applied to the chromatographic column was 2 microlitres. Following the analysis, the peaks obtained were processed using the MultiChrom programme. Consequently, a calibration curve of dye concentration (mg mL^{-1}) *versus* absorbance was obtained, with a correlation coefficient of R = 0.9998, described by the equation $Q = 0.0234 \times A$. The elution time of the dye was found to be 9.17 minutes.

Determination of fluorescence quantum yields of dyes and nanoparticles

In order to determine the quantum yields of the dyes, a series of solutions of dyes **1–8** and selected standards were prepared. For dyes **1–4** containing a morpholine substituent, coumarin 6 dissolved in ethanol was utilised as a standard, characterised by $\lambda_{\max}^{\text{abs}}$ = 457 nm, $\lambda_{\max}^{\text{fl}}$ = 500 nm, Φ_{f} = 78%. For dyes **5–8** containing an ethoxyethyl substituent, quinine sulphate in 0.5 M sulphuric acid was utilised, $\lambda_{\max}^{\text{abs}}$ = 317 and 349 nm, $\lambda_{\max}^{\text{fl}}$ = 450 nm, Φ_{f} = 54,6%.

For compounds **1–4**, the absorption and fluorescence spectra were recorded upon excitation with light at a wavelength of 405 nm, and for **5–8** at a wavelength of 360 nm. The quantum yield of fluorophores was calculated using the following eqn (1):

$$\varphi_{\text{fl}} = \varphi_{\text{st}} \times \frac{S_{\text{fl}}}{S_{\text{st}}} \times \left(\frac{1 - 10^{A_{\text{st}}}}{1 - 10^{A_{\text{fl}}}}\right) \times \left(\frac{n_{\text{fl}}}{n_{\text{st}}}\right)^2, \tag{1}$$

where φ_{fl} and φ_{st} are the quantum yields of fluorescence of the fluorophore and standard, S_{fl} and S_{st} are the integral intensities of fluorescence of the fluorophore and standard, A_{fl} and A_{st} are the absorptions of the fluorophore and standard, n_{fl} and n_{st} are the refractive indices of the medium.

In order to determine the quantum yields of fluorescence of nanoparticles, a series of suspensions with different dilutions were prepared. The conditions for the recording of the spectra remained unchanged, as for the initial fluorophores. Subsequently, graphs were constructed to demonstrate the dependence of the integral fluorescence intensity on absorption at a selected wavelength. The slope coefficients of these graphs were subsequently determined. The following eqn (2) was utilised to calculate the quantum yield of fluorescence of nanoparticles:

$$\varphi_{\mathrm{NPs}} = \varphi_{\mathrm{st}} \times \frac{tg\alpha_{\mathrm{NP}}}{tg\alpha_{\mathrm{st}}} \times \left(\frac{n_{\mathrm{NP}}}{n_{\mathrm{st}}}\right)^2, \quad (2)$$

where φ_{NPs} and φ_{st} are the quantum yields of fluorescence for nanoparticles and the standard, $tg\alpha_{\mathrm{NP}}$ and $tg\alpha_{\mathrm{st}}$ are the tangents of the angle of inclination of the dependence of the integral fluorescence intensity on absorption for nanoparticles and the standard, n_{NP} and n_{st} are the refractive indices of the medium, which are 1.333 for PBS, 1.397 for 0.5 M sulphuric acid solution, and 1.4242 for 96% ethyl alcohol solution.

For all nanoparticles, the values of sample brightness were determined calculated according to eqn (3):

$$B = \varepsilon \cdot \mathrm{QY} \cdot n, \quad (3)$$

where ε is the molar extinction coefficient of the dye, determined by the Beer–Bouguer–Lambert law, $\mathrm{l\ mol^{-1}\ cm^{-1}}$. φ_{NPs} is the quantum yield of fluorescence of nanoparticles. n is the amount of substance of fluorophore molecules per mg of PLGA, $\mathrm{mol\ mg^{-1}}$.

Study of the average lifetime of the excited state of fluorophores in free form and as part of nanoparticles using FLIM microscopy

The registration of colloid systems fluorescence spectra and further registration of the time-resolved signal were performed in two-photon excitation mode using a Cameleon Ultra II femtosecond laser (Coherent, USA), tunable in the range of 690–1060 nm. The excitation of fluorescence was accomplished through the utilisation of a laser wavelength of 770 nm. The fluorescence decay was approximated using a one-, two-, or three-component exponential function.

Preparation of 4T1 cell line

The 4T1 breast adenocarcinoma cell line was selected for *in vitro* study of nanoparticle distribution. The 4T1 cells were cultivated at a temperature of 37 °C in an atmosphere containing 5% CO_2, in RPMI-1640 medium with 10% fetal bovine serum, 2 mM L-glutamine, and 1% antibiotic–antimycotic mixture (10 000 IU per mL penicillin, 10 000 IU per mL streptomycin). The 4T1 cells were cultivated in confocal dishes with lids and bottoms (3.5 SPL Life Sciences Co., Ltd) until 70% confluence was attained 24 hours prior to the experimental study.

Cytotoxicity assessment using the resazurin assay

To assess cytotoxicity, 4T1 cells were seeded in 96-well plates at a density of 2000 cells per well and cultured for 24 h to allow adhesion. Test nanoparticle suspensions were then added to the culture medium at a ratio of 100 μL old medium per well (inoculation volume) and 100 μL fresh medium containing the nanoparticles. Stock suspensions were prepared in serum-free growth medium, with the final added volume not exceeding 11% of the well volume. Cells were incubated with nanoparticles for 24 h, after which cytotoxicity was evaluated using the resazurin assay. Cells receiving medium without test nanoparticles suspension served as controls.

For the resazurin assay, a 0.2 mM resazurin solution in Earle's balanced salt solution supplemented with 1 g $\mathrm{L^{-1}}$ D-glucose was employed. Culture medium was replaced with resazurin solution, and plates were incubated for 2 h at 37 °C. Fluorescence was measured using excitation and emission wavelengths of 535 nm and 620 nm, respectively, on a Hidex Sense Beta Plus plate fluorometer (Hidex, Finland).

Laser scanning confocal microscopy

Cell lysosomes were stained with LysoTracker Red DND-99 (50 nM, Life Technology, USA) according to the manufacturer's protocol. The cells were incubated with LysoTracker for 10 minutes and washed with PBS. PLGA-**4** nanoparticles were added to the cell culture medium to a final concentration of 100 μg $\mathrm{mL^{-1}}$, and the cells were incubated for 1 hour. A concentration of 200 μg $\mathrm{mL^{-1}}$ was used for PLGA-5 nanoparticles. After incubation, the cells were washed three times with PBS. The study utilized lasers with 405, 488, and 561 emission wavelengths and Plan Apo 20×/0.75 Dic N and Apo TIRF 60×/1.49 oil Dic objectives. Images were scanned sequentially with the following optical pass settings: 405 laser (500–550 nm bandpass filter) and 405 laser (425–475 nm bandpass) for fluorophores **1–4** and fluorophores **5–8**, respectively, with TD optical configuration. Live-cell imaging was performed. Imaging analysis and quantification was performed using NIS Elements AR software.

Cells were grown in an adhesion culture in Dulbecco's modified essential medium (DMEM) with 2 mM glutamine and 4.5 g $\mathrm{L^{-1}}$ glucose (PanEco, Russia) supplemented with 10% fetal bovine serum (HyClone, ThermoScientific, USA) and 1% penicillin + streptomycin in a humidified atmosphere under 37 °C and 5% CO_2.

Twenty-four hours before transfection, cells were seeded on glass bottom culture dishes (Fluorodish, World Precision Instruments, USA). For transient transfection, the transfection reagent FuGene HD (Promega, USA) was used in accordance with the manufacturer's protocol. The transfection mixture was diluted with 700 μL of OptiMEM (Gibco, ThermoScientific, USA), and incubation was continued for 16–24 h.

For live-cell imaging using Nanoimager S cells were transfected with plasmids, encoding LAMP1-mScarlet or mKate2-clathrin under CMV promoter and SV40 terminator control. Transfected cells were imaged in HHBS (Hank's HEPES buffer solution, PanEco, Russia). PLGA-**4** nanoparticle suspension was added to a final concentration 100 μg $\mathrm{mL^{-1}}$ and incubated for 30 min.

Determining colocalization coefficients

A preliminary assessment of colocalization between nanoparticles and trackers was performed across the entire image. Manders' and Pearson's coefficients were used to assess colocalization. Coefficients greater than 0.5 indicate colocalization between channels (maximum 1.0).

Study of photostability of nanoparticles PLGA-4 and PLGA-5

To study the relative stability under biological imaging conditions PLGA-Cy5 nanoparticles were used as a control. The PLGA-**4** nanoparticle suspension was incubated with the 4T1 cells at a concentration of 200 μg mL^{-1} for 30 min. The cells were washed twice with phosphate-buffered saline to remove unbound nanoparticles. The cells were then transferred to the confocal microscope (Nikon A1R MP inverted microscope) and and continuously exposed for 7 min (405 nm laser for naphthalimide 5; 637 nm for Cy5; ∼4.7 mW cm^{-2}).

For controlled single-wavelength study the cells were stained with the DAPI dye after fixation. The cells were fixed with 4% formaldehyde solution in PBS (incubated for 10 min at room temp protecting from light). Then the cells were washed twice with PBS and incubated with DAPI (ready to use solution, Sigma Aldrich). The cells were washed twice with PBS and imaging. The dye **4** was dissolved in an aliquot of DMSO, the final DMSO concentration in the cell medium did not exceed 1%. For nanoparticles PLGA-**4** incubated with cells at a concentration of 200 μg mL^{-1} PLGA, the concentration of free dye in the experiments corresponded to the concentration in the PLGA nanoparticles. Cells were fixed under similar conditions. The selected ROI (with representative cells) was bleached for 9 min with a 405 laser (∼4.7 mW cm^{-2}) and the fluorescent intensity from this ROI was measured over time.

Author contributions

Yuriev Danil and Tkachenko Sergey designed and conducted the experiments, conceived the idea and wrote the original manuscript. Ermolin Danila and Ivanov Ilya conducted the TD-DFT and ESD experiments. Melnikov Pavel, Malinovskaya Julia, Mishin Alexander and Perfilov Maxim conducted the fluorescence visualisation experiments. Ryabova Anastasia conducted the FLIM microscopy experiments. Khasbiullin Ramil conducted the DSC experiments. Medvedev Mikhail and Skorb Ekaterina supervised the TD-DFT and ESD experiments. Oshchepkov Maxim, Gelperina Svetlana and Oshchepkov Alexander supervised the work, provided resources and reviewed the manuscript. All authors contributed to the discussion and analysis of the results.

Conflicts of interest

There are no conflicts to declare.

Data availability

The Supplementary information (SI) for this article contains detailed characterization data supporting the findings of this study, including: structural and purity verification: NMR (^{1}H, ^{13}C) and IR spectra of PLGA and conjugates, GPC chromatograms, DSC thermograms, and HPLC purity analysis of the synthesized polymers. Computational methodology: detailed DFT/TD-DFT calculation parameters and comparison between experimental and predicted spectra (absorption/fluorescence) for all fluorophore derivatives. Photophysical and stability data: comprehensive spectral characterization (extinction coefficients, fluorescence spectra in CH_2Cl_2, DMSO, and H_2O), brightness comparisons with commercial markers, and stability studies (size/fluorescence intensity) in biological media (PBS, RPMI-1640, DMEM). Biological evaluation: cytotoxicity assay details (Alamar Blue) and standardized photostability benchmarking (time-dependent profiles) against common commercial fluorophores. All experimental and computational data are provided to ensure the reproducibility and technical transparency of the reported naphthalimide-PLGA platform. See DOI: https://doi.org/10.1039/d5tb02866c.

Notes and references

1 O. C. Adekoya, G. J. Adekoya and E. R. Sadiku, *Pharmaceutics*, 2022, **14**, 1972.
2 H. Guan, H. Sun and X. Zhao, *Int. J. Mol. Sci.*, 2025, **26**, 3262.
3 J.-J. Zheng, *Chem. Soc. Rev.*, 2024, **53**, 9059–9132.
4 J. Yang, H. Zeng and Y. Luo, *Polymers*, 2024, **16**, 2606.
5 M. Chatterjee and N. Chanda, *Mater. Adv.*, 2022, **3**, 837–858.
6 J. M. Lababidi and H. M. E. S. Azzazy, *NPJ Parkinsons Dis.*, 2025, **11**, 248.
7 M. B. Giles, J. K. Y. Hong and Y. Liu, *Nat. Commun.*, 2022, **13**, 3282.
8 A. Areny Balagueró, W. Mekseriwattana and M. Camprubí-Rimblas, *Pharmaceutics*, 2022, **14**, 1447.
9 M. Chatterjee, R. Maity, S. Das, N. Mahata, B. Basu and N. Chanda, *Mater. Adv.*, 2020, **1**, 3033–3048.
10 V. Zhukova, N. Osipova and A. Semyonkin, *Pharmaceutics*, 2021, **13**, 1145.
11 Z. Shahroosvand, N. R. Yeganeh and S. Haddadian, *Appl. Nanosci.*, 2020, **10**, 1441–1452.
12 Y. Zhang, J. Zhou and D. Guo, *Int. J. Nanomed.*, 2013, **8**, 3745–3756.
13 E. Zhang, V. Zhukova and A. Semyonkin, *Eur. J. Pharm. Biopharm.*, 2020, **150**, 131–142.
14 N. Williams Nkune, K. Moloudi and B. P. George, *RSC Adv.*, 2025, **15**, 22267–22284.
15 E. Balaburov, M. Kamaraj and S. E. Doyle, *J. Appl. Polym. Sci.*, 2024, **141**, e54759.
16 Y. Fu, X. Zhang, L. Wu, M. Wu, T. D. James and R. Zhang, *Chem. Soc. Rev.*, 2025, **54**, 201–265.
17 A. Areny-Balagueró, W. Mekseriwattana and M. Camprubí-Rimblas, *Pharmaceutics*, 2022, **14**, 1447.
18 S. B. Aziz, M. A. Brza and M. M. Nofal, *Materials*, 2020, **13**, 3675.
19 S. Shafiq and K. Walczak, *Org. Biomol. Chem.*, 2025, **23**, 6287–6319.
20 H. Yu, Y. Guo and W. Zhu, *Coord. Chem. Rev.*, 2021, **444**, 214019.
21 W. Nie and L. Hu, *ChemistrySelect*, 2024, **9**, e202303779.
22 Y. Dai, H. Huang and H. Gao, *J. Mol. Struct.*, 2025, **1340**, 142529.
23 A. Oshchepkov, M. S. Oshchepkov, M. V. Oshchepkova and E. A. Kataev, *Adv. Opt. Mater.*, 2021, **9**, 2001913.

24 S. Kotowicz, J. G. Małecki and A. K. Pająk, *J. Mol. Struct.*, 2025, **1332**, 141711.

25 I. Grabchev, S. Angelova and D. Staneva, *Inorganics*, 2023, **11**, 47.

26 C. J. Christopherson, D. M. Mayder and J. Poisson, *ACS Appl. Mater. Interfaces*, 2020, **12**, 20000–20011.

27 V. Petkova, D. Anastasova and S. Dobrev, *Molecules*, 2024, **29**, 4204.

28 G. Kozalak, S. H. Davoudian and E. Natsaridis, *Micromachines*, 2025, **16**, 972.

29 M. Kuddushi, C. Kanike and B. B. Xu, *Soft Matter*, 2025, **21**, 2759–2781.

30 L. Toms, L. FitzPatrick and P. Auckland, *SLAS Discovery*, 2025, **31**, 100209.

31 S. Pujals and L. Albertazzi, *ACS Nano*, 2019, **13**, 9707–9712.

32 D. Jin, P. Xi and B. Wang, *Nat. Methods*, 2018, **15**, 415–423.

33 Y. Qu, L. Wang and J. Wu, *Dyes Pigm.*, 2017, **148**, 99–107.

34 A. Chevalier, *Org. Biomol. Chem.*, 2023, **21**, 7498–7510.

35 Y. Dai, H. Gao and H. Huang, *Anal. Methods*, 2025, **17**, 9823–9832.

36 C. Zhou, Y. Zhang, Y. Sun and L. Yan, *J. Mol. Struct.*, 2026, **1349**, 143604.

37 M. Oshchepkov, S. Tkachenko and K. Popov, *Dyes Pigm.*, 2024, **231**, 112386.

38 R. F. Salikov, K. P. Trainov and D. N. Platonov, *Dyes Pigm.*, 2019, **161**, 500–509.

39 B. de Souza, F. Neese and R. Izsák, *J. Chem. Phys.*, 2018, **148**, 034104.

40 W. Huang and C. Zhang, *Biotechnol. J.*, 2018, **13**, e1700203.

41 D. Panigrahi, P. K. Sahu and S. Swain, *SN Appl. Sci.*, 2021, **3**, 638.

42 C. B. Roces, D. Christensen and Y. Perrie, *Drug Discovery Transl. Res.*, 2020, **10**, 582–593.

43 A. Pucek-Kaczmarek, *Processes*, 2021, **9**, 1265.

44 P. Zhang, X. Guo and Y. Xiao, *Spectrochim. Acta, Part A*, 2019, **223**, 117318.

45 L. Meng, X. Ma and S. Jiang, *CCS Chem.*, 2021, **3**, 2084–2094.

46 P. A. López and S. A. Blum, *ACS Catal.*, 2024, **14**, 17132–17147.

47 H. Lin, *Semin. Ophthalmol.*, 2016, **31**(1), 1–9.

48 C. V. Rocha, *Int. J. Mol Sci.*, 2022, **23**(4), 203.

49 T. W. L. Barbosa, *Molecules*, 2025, **30**(8), 1818.

50 I. Kelmanson, *Nat. Methods*, 2009, **6**, iii–iv.

51 C. Palocci, A. Valletta and L. Chronopoulou, *Plant Cell Rep.*, 2017, **36**, 1917–1928.

52 J. Mahmoudian and R. Hadavi, *Cell J.*, 2011, **13**, 169–172.

53 X. Li, J. Bian and M. Fu, *Anal. Methods*, 2022, **14**, 1279–1284.

54 J. Sasikumar, S. Laha and B. Naik, *Sci. Rep.*, 2024, **14**, 20936.

55 J. Bucevičius, G. Lukinavičius and R. Gerasimaitė, *Chemosensors*, 2018, **6**(2), 18–25.

56 P. Pracht, F. Bohle and S. Grimme, *Phys. Chem. Chem. Phys.*, 2020, **22**, 7169–7192.

57 C. Bannwarth, S. Ehlert and S. Grimme, *J. Chem. Theory Comput.*, 2019, **15**, 1652–1671.

58 S. Ehlert, M. Stahn and S. Spicher, *J. Chem. Theory Comput.*, 2021, **17**, 4250–4261.

59 F. Neese, *Wiley Interdiscip. Rev.: Comput. Mol. Sci.*, 2022, **12**, e1606.

60 C. Adamo and V. Barone, *J. Chem. Phys.*, 1999, **110**, 6158–6170.

61 E. Caldeweyher, J.-M. Mewes and S. Ehlert, *Phys. Chem. Chem. Phys.*, 2020, **22**, 8499–8512.

62 M. K. Kesharwani, B. Brauer and J. M. L. Martin, *J. Phys. Chem. A*, 2015, **119**, 1701–1714.